A real-time wave prediction in directional wave fields: Strategies for accurate continuous prediction in time

I.-C. Kim, G. Ducrozet, Leroy Vincent, F. Bonnefoy, Y. Perignon, Sébastien Bourguignon

▶ **To cite this version:**

I.-C. Kim, G. Ducrozet, Leroy Vincent, F. Bonnefoy, Y. Perignon, et al.. A real-time wave prediction in directional wave fields: Strategies for accurate continuous prediction in time. Ocean Engineering, 2024, 291, pp.116445. 10.1016/j.oceaneng.2023.116445 . hal-04327971

HAL Id: hal-04327971
https://hal.science/hal-04327971v1

Submitted on 5 Mar 2024

HAL is a multi-disciplinary open access archive for the deposit and dissemination of scientific research documents, whether they are published or not. The documents may come from teaching and research institutions in France or abroad, or from public or private research centers.

L'archive ouverte pluridisciplinaire **HAL**, est destinée au dépôt et à la diffusion de documents scientifiques de niveau recherche, publiés ou non, émanant des établissements d'enseignement et de recherche français ou étrangers, des laboratoires publics ou privés.

Distributed under a Creative Commons Attribution - NonCommercial - NoDerivatives 4.0 International License

Ocean Engineering 291 (2024) 116445

Contents lists available at ScienceDirect

Ocean Engineering

journal homepage: www.elsevier.com/locate/oceaneng

Research paper

A real-time wave prediction in directional wave fields: Strategies for accurate continuous prediction in time

I.-C. Kim [a,c,*], G. Ducrozet [a], V. Leroy [a], F. Bonnefoy [a], Y. Perignon [a], S. Bourguignon [b]

[a] Nantes Université, École Centrale Nantes, CNRS, LHEEA, UMR 6598, F-44000 Nantes, France
[b] Nantes Université, École Centrale Nantes, CNRS, LS2N, UMR 6004, F-44000 Nantes, France
[c] College of Earth, Ocean, and Atmospheric Sciences, Oregon State University, Corvallis, OR, USA

ARTICLE INFO

Dataset link: https://doi.org/10.5281/zenodo.7689781

Keywords:
Ocean waves
Phase-resolved model
Real-time prediction
Data assimilation
Directional wave
Wave tank experiments

ABSTRACT

Previous research on real-time deterministic sea wave prediction has generally focused on evaluating the accuracy and efficiency of short-term wave fields within a specific prediction zone. However, for a real-time wave prediction system, it is necessary to provide a continuous description of the ocean wave surface based on short-term prediction segments. In this regard, we have developed algorithms for continuous wave prediction in directional wave fields based on the "practical" prediction zone. The practical prediction zone refers to the time interval available for generating a continuous wave forecast by excluding the reconstructed waves from the prediction zone proposed by Kim et al. (2023). We also introduce and discuss several important time factors, such as the update interval of the spatio-temporal wave dataset, the total computation time, and the length of the practical prediction zone. By gaining a deeper understanding of numerical modeling setups, we have established strategies to reduce computational costs, which are directly related to the accuracy of continuous wave prediction. In particular, the development of these strategies suggests guidance in specifying direction and frequency bandwidths for continuous wave prediction.

1. Introduction

A real-time short-term deterministic sea wave prediction, aiming to provide wave descriptions several tens of seconds before waves arrive at floating structures, is important for the safety and efficiency of surface vessel operations (Grilli et al. 2011, Nouguier et al. 2013, Kusters et al. 2016, Dannenberg et al. 2010). It can also improve ocean wave energy harvesting systems (Li et al. 2012, Previsic et al. 2021) and the design of marine structures, such as floating wind turbines (Raach et al. 2014, Ma et al. 2018, Al et al. 2020). The present work was supported by the European H2020 FLOATECH and French ANR CREATIF projects. In this project, real-time wave forecasts are implemented for optimizing actions on structures, such as load mitigation on offshore floating wind turbines. We herein develop algorithms for a continuous (in time) description of the ocean wave surface based on short-term wave prediction.

Some operational systems for the floating structure in actual sea states require a continuous exchange of wave information (Lee et al., 2022). With constantly provided inputs (e.g., spatio-temporal datasets), a series of short-term predictions can be generated. Here, short-term prediction refers to a limited wave description of the future over a specific domain in time and space. When using a set of short-term ocean waves to provide a continuous (long-term) wave prediction *in time*, we should optimize the prediction system by considering computational time, the presence of overlapping waves between short-term segments, and their corresponding accuracy. Nonetheless, to our knowledge, the influence of numerical modeling setups focusing on the final continuous prediction has not yet been studied. In most instances to date, studies on the problems of short-term wave prediction have primarily dealt with the accuracy of the algorithms within the limited prediction horizon. Efforts toward achieving real-time simulation with a low computational cost have also been made by developing efficient data assimilation processes (e.g., Köllisch et al. 2018, Al-Ani et al. 2019, Kim et al. 2023) or using machine learning methods (e.g., Law et al. 2020, Duan et al. 2020, Zhang et al. 2022b).

In this work, we discuss the challenges associated with the continuous (in time) description of ocean wave motion. The primary focus of our model performance assessment presented here is on the basis of accurately describing the continuous wave profile prediction, rather than short-term wave prediction. In this regard, we investigate the impact of temporal quantities, such as the length of the prediction zone in time and the computation time, on the accuracy of continuous wave prediction. Depending on the magnitude of these factors, the long-term

* Corresponding author at: College of Earth, Ocean, and Atmospheric Sciences, Oregon State University, Corvallis, OR, USA.
E-mail address: inchul.kim@oregonstate.edu (I.-C. Kim).

https://doi.org/10.1016/j.oceaneng.2023.116445
Received 12 July 2023; Received in revised form 25 October 2023; Accepted 24 November 2023
0029-8018/© 2023 The Authors. Published by Elsevier Ltd. This is an open access article under the CC BY-NC-ND license (http://creativecommons.org/licenses/by-nc-nd/4.0/).

Nomenclature

Acronyms

CWM	Choppy wave model
ICWM	Improved choppy wave model
ISSP	Improved surface similarity parameter
LIDAR	Light detection and ranging
LWT	Linear wave theory
LWT-CDR	Linear wave theory with a corrected dispersion relationship
SSP	Surface similarity parameter
WG21	Additional downstream wave gauge or target location

Greek Symbols

$\bar{\eta}_l$	Measured surface elevation at the lth measurement point
β_a	Horizontal aperture angle ($=2\theta_B$)
η	Free surface elevation
η_l	Simulated surface elevation at the lth measurement point
μ	Small fraction of wave spectrum
$\omega_{\max}$	Maximum wave frequency
$\omega_{\min}$	Minimum wave frequency
ω_p	Peak wave angular frequency
ω_{n_ω}	Wave angular frequency
Ψ_n	Nonlinear phase function
ψ_n	Linear phase function
τ	Time interval between measured surface samples
θ	Propagation direction
$\theta_{\lim}$	Direction limit or half of direction bandwidth
$\theta_{\max}$	Maximum direction cutoff
$\theta_{\min}$	Minimum direction cutoff
θ_B	Angle between both end directional arrays
θ_{n_θ}	Propagation direction for the n_θ direction component
$\tilde{\omega}_n$	Corrected wave frequency
$\tilde{\psi}_n$	Corrected nonlinear phase function
ε	Normalized misfit error
ε^{CP}	Averaged normalized misfit error over the entire duration
ε^{PP}	Averaged normalized misfit error over the practical prediction zone
Δt	Time step of wave observations
$\eta_{pred,i}$	Prediction ocean surface of the ith sample
$\eta_{ref,i}$	Reference ocean surface of the ith sample

Other Symbols

$\lceil\ \rceil$	Least integer function

Roman Symbols

$\mathbf{A}$	Coefficient matrix
$\mathbf{B}$	Measurement matrix
$\mathbf{k}_n$	Wavenumber vector
$\mathbf{p}$	Amplitude parameter vector
$\mathbf{r}$	Horizontal coordinate vector
$\mathbf{r}_j$	Horizontal coordinate vector at the jth spatial measurement point
$\mathbf{U}_{s0}$	Stokes drift
$\mathfrak{T}$	Length of practical prediction zone ($= t_{\max} - t_r$)
$\overline{F}_{\eta,ref}$	Frequency-averaged Fourier transform of reference surface elevations
A_n	Wave amplitude
a_n	First wave amplitude parameter
b_n	Second wave amplitude parameter
$c_{g,\max}$	Maximum group velocity
$c_{g,\min}$	Minimum group velocity
c_{g,N_ω}	Group velocity of the last frequency component
d	Water depth
$F(\mathbf{p})$	Quadratic cost function
f_p	Peak wave frequency
$F_{\eta,pred}$	Fourier transform of prediction surface elevations
$F_{\eta,ref}$	Fourier transform of reference surface elevations
H_s	Significant wave height
J	Total number of measurement points in space ($= J_r \times J_\theta$)
j	Index for spatial measurement point
J_θ	Total number of directional arrays for measurement zone
J_r	Total number of wave gauges installed on a straight structure
K	Total number of measurement points in time
k	Index for temporal measurement point
k_1	Wavenumber of the first frequency component
k_p	Peak wavenumber
k_{N_ω}	Wavenumber of the last frequency component
L	Total number of spatio-temporal measurement points ($= J \times K$)
l	Index for spatio-temporal measurement point
L_p	Peak wavelength
N	Total number of wave components
n	Index for wave component
N_ω	Total number of wavenumber components
n_ω	Index for wavenumber component
N_θ	Total number of direction components
n_θ	Index for direction component
$N_\theta^{Present}$	Total number of direction components in the present study
$N_\theta^{Previous}$	Total number of direction components in the previous study

forecast may involve overlapping waves. Hence, it becomes necessary to address the issue of overlapping short-term forecasts while improving the representation of wave propagation. Strategies for long-term wave prediction are explored not only in terms of wave parameters in numerical simulations but also in terms of an iterative process of determining the initial wave conditions (e.g., initial guess and error tolerance).

N_s	Number of surface samples
P_{ml}^{LWT}	Derivative of η with respect to a_m at the lth point for LWT
Q_{ml}^{LWT}	Derivative of η with respect to b_m at the lth point for LWT
s	Directional spreading factor
$S_\eta(\omega)$	Power spectral density
t'	Relative time ($= t - t_r$)
$t'_{\max}$	Relative end of prediction zone in time ($= t_{\max} - t_r$)
$t'_{\min}$	Relative beginning of prediction zone in time ($= t_{\min} - t_r$)
t	Time
$t_{\max}$	End of prediction zone in time
$t_{\min}$	Beginning of prediction zone in time
T_a	Assimilation time
t_a	Start of time series used in this study
t_b	End of time series measured in experiments
t_k	Time at the kth temporal measurement point
T_p	Peak period
t_r	Latest time of wave reconstruction
$t_{\max_i}$	End of prediction zone in time for the ith surface sample
$t_{\min_i}$	Beginning of prediction zone in time for the ith surface sample
$T_{forecast}$	Forecast calculation time for a single short-term prediction
$T_{nowcast}$	Nowcast calculation time for a single short-term prediction
t_{r_i}	Latest time of wave reconstruction for the ith surface sample
t_{r_i}	Latest time used in wave reconstruction for the ith surface sample
T_{total}	Total calculation time for a single short-term prediction
x	Spatial coordinate
x_b	x-coordinate of beginning of measurement points
x_e	x-coordinate of end of measurement points
x_t	x-coordinate of target point
y'	Relative y-coordinate with respect to the centerline ($= y - y_c$)
y	Spatial coordinate perpendicular to x
z	Vertical coordinate
$A_{(m,n)}^{LWT}$	Entry in **A** for LWT
$B_{(m,n)}^{LWT}$	Entry in **B** for LWT
$\hat{\mathbf{k}}_{n_\theta}$	Unit wave vector
k_{n_ω}	Wavenumber

Methods for deterministic wave prediction have been developed using wave datasets obtained by LIDAR (Light Detection and Ranging) cameras (e.g., Grilli et al. 2011, Nouguier et al. 2013, Kabel et al. 2019, Desmars et al. 2020). An alternative to the LIDAR technique uses X-band radars (or microwave radars) to record observations of the sea surface elevation (e.g., Hilmer and Thornhill 2015, Kusters et al. 2016, Naaijen et al. 2018, Klein et al. 2020, Zhang et al. 2022a). Both LIDAR and X-band radar measurements, obtained by a structure-mounted instrument with the grazing incidence angles of the beams, have inherent physical limitations, such as uneven spatial sampling. Moreover, a wave shadowing phenomenon is more likely to occur due to the spatial gaps behind the illuminated wavefronts. The insufficiency of data over the shadowed regions may be compensated by using spatio-temporal datasets (e.g., Grilli et al. 2011, Nouguier et al. 2013, Kabel et al. 2019, Desmars et al. 2020).

Nonlinear phase-resolved models can capture detailed nonlinear surface wave dynamics. As the sea states become more severe in terms of wave steepness or when the time horizon of the wave prediction is extended, nonlinear wave mechanics, such as bound waves and nonlinear phase velocity, need to be addressed. In this context, Nouguier et al. (2009) proposed the Choppy Wave Model (CWM) based on the Lagrangian description. Later, Guérin et al. (2019) developed the Improved Choppy Wave Model (ICWM) by redefining the location of reference particles, resulting in a modified third-order nonlinear dispersion relation that is entirely consistent with that of the Eulerian system. Recent comprehensive studies of this topic (Desmars et al. 2020, Kim et al. 2023) showed that wave prediction algorithms based on the Lagrangian approach successfully simulate the propagation of any wave field in real-time with great accuracy for both unidirectional and multidirectional wave conditions.

This paper is organized as follows. In Section 2, we define the methods used to provide the continuous prediction of phase-resolved ocean waves. In particular, Section 2.3 details the continuous wave prediction. Section 3 explains the dedicated wave-tank experiment and the corresponding prediction zone. Strategies to improve model accuracy of the long-term forecast and their effects on prediction errors are presented in Sections 4 and 5, respectively. Finally, we summarize the conclusions of this paper in Section 6.

2. Methods

This section describes how to achieve a continuous wave forecast system based on wave measurements around the target point. The process begins with short-term wave predictions, which consist of two steps: (1) data assimilation (or reconstruction; 'nowcast') that uses wave datasets to initialize the wave models; (2) wave propagation (or prediction; 'forecast') that simulates ocean wave surfaces over the spatio-temporal domain where the short-term wave prediction is valid. The continuous wave prediction system in real-time is constructed by combining the short-term ocean surfaces appropriately.

2.1. Wave models

We used ICWM (Guérin et al., 2019), based on the second-order Lagrangian description, as the most developed wave model due to its inclusion of essential nonlinear aspects. We compare the resulting wave forecasts obtained using ICWM with those obtained using linear wave theory (LWT) and by linear wave theory with a corrected dispersion relationship (LWT-CDR).

2.1.1. LWT

We define a Cartesian coordinate system with $(x, y, z) = (\mathbf{r}, z)$, where (x, y) is located on the mean free surface and z is positive vertically upward. The linearized water wave boundary problem describes the behavior of small steepness waves on the surface of an inviscid and incompressible fluid and an irrotational flow. The free surface elevation at time t by LWT is expressed by:

$$\begin{aligned}\eta^{\mathrm{LWT}}(x,y,t) &= \sum_{n=1}^{N}\left[a_n\cos\psi_n + b_n\sin\psi_n\right] \\ &= \sum_{n_\omega=1}^{N_\omega}\sum_{n_\theta=1}^{N_\theta}\left[a_{(n_\omega,n_\theta)}\cos\psi_{(n_\omega,n_\theta)} + b_{(n_\omega,n_\theta)}\sin\psi_{(n_\omega,n_\theta)}\right]\end{aligned} \tag{1}$$

where subscript n indicates the nth wave component $n = (n_\omega, n_\theta)$, with n_ω and n_θ being the n_ωth wavenumber component ($n_\omega = 1$ to N_ω) and the n_θth direction component ($n_\theta = 1$ to N_θ), respectively. The wave

amplitude parameters (a_n, b_n) are determined by the amplitude A_n and the phase φ_n:

$$(a_n, b_n) = (A_n \cos\varphi_n, A_n \sin\varphi_n) \tag{2}$$

and the linear phase function is

$$\psi_n = \mathbf{k}_n \cdot \mathbf{r} - \omega_n t = k_{n_\omega} \cos\theta_{n_\theta} x + k_{n_\omega} \sin\theta_{n_\theta} y - \omega_{n_\omega} t \tag{3}$$

where $\mathbf{k}_n = k_{n_\omega} \hat{\mathbf{k}}_{n_\theta}$ is the wavenumber vector, in which the unit wave vector $\hat{\mathbf{k}}_{n_\theta} = (\cos\theta_{n_\theta}, \sin\theta_{n_\theta})$ is given by the propagation direction θ_{n_θ}. The wavenumber k_{n_ω} and the wave frequency ω_{n_ω} are related by the linear dispersion relation in deep water. For a finite water depth, we can easily obtain a similar equation by using the fully dispersive wavenumber.

2.1.2. ICWM

Guérin et al. (2019) proposed ICWM on the basis of the Lagrangian formalism, and ICWM has been proven to be advantageous for solving the propagation of nonlinear waves at a low numerical cost (Desmars et al. 2020, Kim et al. 2023). The surface elevation is explicitly given by ICWM:

$$\eta^{\mathrm{ICWM}}(x, y, t) = \sum_{n=1}^{N} [a_n \cos\Psi_n + b_n \sin\Psi_n + \frac{1}{2}(a_n{}^2 + b_n{}^2) k_n] \tag{4}$$

where the nonlinear phase function Ψ_n represents critical contributions to the nonlinear wave effects: the nonlinear phase shift represented by the summation in Eq. (5) and Stokes drift $\mathbf{U}_{s0}$:

$$\Psi_n = \mathbf{k}_n \cdot [\mathbf{r} - \sum_{i=1}^{N} \hat{\mathbf{k}}_i (-a_i \sin\tilde{\psi}_i + b_i \cos\tilde{\psi}_i)] - \tilde{\omega}_n t \tag{5}$$

$$\mathbf{U}_{s0} = \sum_{i=1}^{N} (a_i{}^2 + b_i{}^2) \omega_i \mathbf{k}_i \tag{6}$$

where a tilde denotes quantities with the effect of Stokes drift, such as the corrected wave angular frequency $\tilde{\omega}_n = \omega_n + \frac{1}{2}\mathbf{k}_n \cdot \mathbf{U}_{s0}$ and the corrected nonlinear phase function $\tilde{\psi}_n = \mathbf{k}_n \cdot \mathbf{r} - \tilde{\omega}_n t$. The last term in Eq. (4) refers to a correction of the mean surface level.

2.1.3. LWT-CDR

The model based on linear wave theory with the corrected dispersion relation (LWT-CDR) was also taken into account in this paper. Due to the inclusion of the effect of Stokes drift only, it also provides a good compromise between simplicity and accuracy. We note that the nonlinear wave models employed in this paper (i.e., LWT-CDR and ICWM) are based on the same assumptions as in LWT. The free surface by LWT-CDR is

$$\eta^{\mathrm{LWT\text{-}CDR}}(x, y, t) = \sum_{n=1}^{N} [a_n \cos\tilde{\psi}_n + b_n \sin\tilde{\psi}_n] \tag{7}$$

2.2. Data assimilation

The amplitude parameters (i.e., a_n and b_n) in the wave models are obtained through the process of model inversion using the measured surface elevation $\bar{\eta}_l$, assuming unchanging wave parameters over the prediction zone. In the present study, a quadratic cost function measuring the discrepancy between the measured surface elevation $(\bar{\eta}_l)$ and the simulated one (η_l) is employed in the data assimilation process (Blondel et al., 2010), and we aim to minimize the least squares cost function with respect to a_n and b_n:

$$F(\mathbf{p}) = \frac{1}{2} \sum_{l=1}^{L} [\eta_l(\mathbf{p}) - \bar{\eta}_l]^2 = \frac{1}{2} \sum_{j=1}^{J} \sum_{k=1}^{K} [\eta_{(j,k)}(\mathbf{p}) - \bar{\eta}_{(j,k)}]^2 \tag{8}$$

where $\mathbf{p} = [a_1, \ldots, a_N, b_1, \ldots, b_N]^T$ is the vector composed of amplitude parameters. Subscript ℓ denotes the ℓth spatio-temporal measurement point $\ell = (j, k)$ ($\ell = 1$ to L) at the spatial point $\mathbf{r}_j$ ($j = 1$ to J) and time t_k ($k = 1$ to K). The total number of spatio-temporal data is $L = J \times K$. As the system of equations $\mathbf{Ap} = \mathbf{B}$, or the coefficient matrix $\mathbf{A}$ and the measurement matrix $\mathbf{B}$ vary depending on the wave model, we present them for each wave model in this section.

2.2.1. LWT

The matrices in the process of data assimilation for LWT are represented by:

$$\begin{aligned}
A^{LWT}_{(m,n)} &= \sum_{l=1}^{L} \cos\psi_{nl} P^{LWT}_{ml} \\
A^{LWT}_{(m,N+n)} &= \sum_{l=1}^{L} \sin\psi_{nl} P^{LWT}_{ml} \\
A^{LWT}_{(N+m,n)} &= \sum_{l=1}^{L} \cos\psi_{nl} Q^{LWT}_{ml} \\
A^{LWT}_{(N+m,N+n)} &= \sum_{l=1}^{L} \sin\psi_{nl} Q^{LWT}_{ml} \\
B^{LWT}_{m} &= \sum_{l=1}^{L} \bar{\eta}_l P^{LWT}_{ml} \\
B^{LWT}_{N+m} &= \sum_{l=1}^{L} \bar{\eta}_l Q^{LWT}_{ml}
\end{aligned} \tag{9}$$

with

$$P^{LWT}_{ml} = \cos\psi_{ml}, Q^{LWT}_{ml} = \sin\psi_{ml} \tag{10}$$

where $(n, m) \in \{1, \ldots, N\}^2$ and $\psi_{ml} = \mathbf{k}_{ml} \cdot \mathbf{r}_l - \omega_m t_l$. For brevity, we omit the explanation of the regularization to cope with an ill-conditioned inverse reconstruction problem resulting from practical constraints (e.g., the limited zone measured by the optical sensor).

2.2.2. Nonlinear assimilation

Compared to the linear assimilation procedure, ICWM as well as LWT-CDR involve an even more complicated data assimilation with an iterative process owing to the nonlinear phase function Ψ_n containing a_n and b_n. Kim et al. (2023) thus simplified the nonlinear assimilation to obtain results faster than real-time by discarding nonlinear terms influenced by a_n and b_n in part of $\mathbf{A}$ and $\mathbf{B}$.

As $\mathbf{A}$ and $\mathbf{B}$ are influenced by the amplitude parameters, the solutions are found iteratively. In Kim et al. (2023), the iterative process was performed with a maximum iteration number of 100 and a relative tolerance of 10^{-3}. In cases where the convergence was too slow or even unreached, the solution to linear assimilation was used instead of the nonlinear solution. In this study, a tolerance of 10^{-2} was used since there were no changes in the results. The maximum iteration number was reduced from 100 to 20 with a tolerance of 10^{-2} to avoid unnecessary iterations, as the average number of iterations required to reach convergence was around 10. All cases requiring 20 iterations finally diverged. In this study, we utilized the solution of the previous surface sample as an initial guess for the amplitude parameters, which was obtained directly from the linear solution in previous studies (e.g., Desmars et al. 2020, Kim et al. 2023). The next section will provide a definition of the surface sample.

2.3. Continuous wave prediction

2.3.1. Short-term wave prediction

The spatio-temporal wave observations can be utilized to provide short-term wave prediction at the target point x_t, as shown in Fig. 1. The color bar at the top of the figures indicates the short-term prediction. The gold rectangle represents the spatio-temporal wave measurements, spanning from the beginning x_b to the end x_e of measurement points in the x-direction (or the main propagation direction) over $[t_r - T_a, t_r]$. Here, t_r corresponds to the latest time used in wave

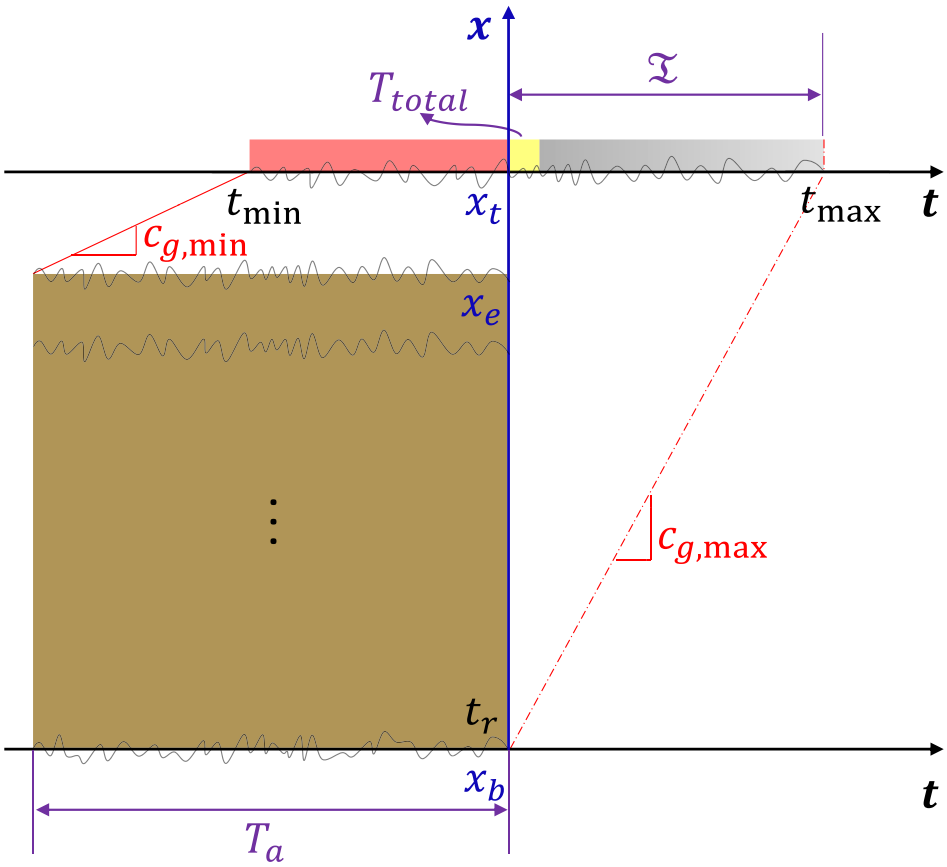

Fig. 1. Short-term deterministic sea wave prediction at x_t based on measurements between x_b and x_e over T_a (——: line with slope $c_{g,\min}$; —·—: line with slope $c_{g,\max}$; gold rectangle: assimilated data; red shading: reconstruction over $t \in [t_{\min}, t_r]$; yellow shading: computation over $t \in [t_r, t_r + T_{total}]$; gray shading: useful prediction zone over $t \in [t_r + T_{total}, t_{\max}]$).

reconstruction, and T_a refers to the assimilation time. The abscissa t represents the temporal coordinate, where the time at the origin indicates the latest time of assimilated data (i.e., $t = t_r$). The ordinate x denotes the spatial coordinate along the wave propagation direction, with the origin corresponding to the beginning of the measurement points (i.e., $x = x_b$). The figures explain the case based on multiple fixed points for unidirectional waves, and the extension to directional waves is straightforward.

Previous studies have demonstrated that when wave measurements are provided in a limited domain in time and space, the description of the wave field is confined to a short-term prediction zone determined by the group velocities and propagation directions of wave components (Naaijen et al. 2014, Qi et al. 2018b). In general, the wave frequency cutoffs $\omega_{\min}$ and $\omega_{\max}$ are defined based on the wave spectral density used for generating wave fields, and the corresponding group velocities $c_{g,\max}$ and $c_{g,\min}$ are computed using the linear dispersion relation in deep water. The selection of the wave frequency and direction cutoffs will be detailed in Section 3.2. At the target point x_t, the prediction zone is delimited by red diagonal lines in Fig. 2, whose slopes are the group velocities. The intersection of the solid red line (with a slope $c_{g,\min}$) and $x = x_t$ indicates the reconstruction of the prespecified wave packet from the instant $t_{\min}$. Besides, the dashed lines (with a slope $c_{g,\max}$) are drawn from the basis of the measurement rectangles or $x = x_b$ since the final instant of the prediction time horizon $t_{\max}$ is determined by the fastest wave component within the wave packet.

We introduce here several key terminologies in time. The total calculation time for a single short-term prediction, denoted as T_{total}, is the sum of the nowcast time $T_{nowcast}$ and the forecast time $T_{forecast}$. In general, the nowcast time is significantly longer than the forecast time (Köllisch et al. 2018, Kim et al. 2023). The length of the practical prediction zone, referred to as $\mathfrak{T}$, is primarily determined by the maximum group velocity and the distance between x_b and x_t.

The reconstructed wave information at $t < t_r$ (indicated by the red shading in the figures) is not available for practical continuous wave prediction. Therefore, we define $t \in [t_r, t_{\max}]$ (or $t' = t - t_r \in [0, t'_{\max} = t_{\max} - t_r]$ where $t'_{\max} = \mathfrak{T}$) as the "practical" prediction zone, which represents the actual time interval utilized in operating a real-time system for continuous wave forecasting. The figures also highlight two beneficial aspects of using spatio-temporal data with respect to the practical prediction zone. First, due to the advection of the first wave field during T_a, the reconstructed waves arrive at the target point x_t before the beginning of the forecast step (i.e., $t_{\min} < t_r$), provided that the distance between x_e and x_t is within a certain allowable range: $x_t - x_e < c_{g,\min} T_a$. Second, the use of multiple fixed points extends the time horizon compared to measurements from a single fixed point (i.e., at x_e).

In addition to the reconstruction period, wave forecasting is unavailable during the computation period, as indicated by the yellow shading. Consequently, we refer to the shorter interval over $t \in [t_r + T_{total}, t_{\max}]$ (or $t' \in [T_{total}, \mathfrak{T}]$) as the "useful" prediction zone, which is indicated by the gray shading in the figures. The gray-scale spectrum expresses the model accuracy, which worsens as time increases within the short-term wave prediction. The temporal evolution of prediction error will be presented in later sections (e.g., Fig. 12). The brighter the shade, the greater the prediction error.

2.3.2. Overview of continuous wave prediction

Figs. 2 and 3 provide an overview of the process for obtaining continuous ocean waves at x_t by combining a series of short-term deterministic sea wave predictions. The time interval between sets of the spatio-temporal wave measurements (or measured surface samples) is denoted as τ. In the case of radar images, this interval corresponds to the radar rotation period (Lee et al., 2022). Thus, the partly overlapping

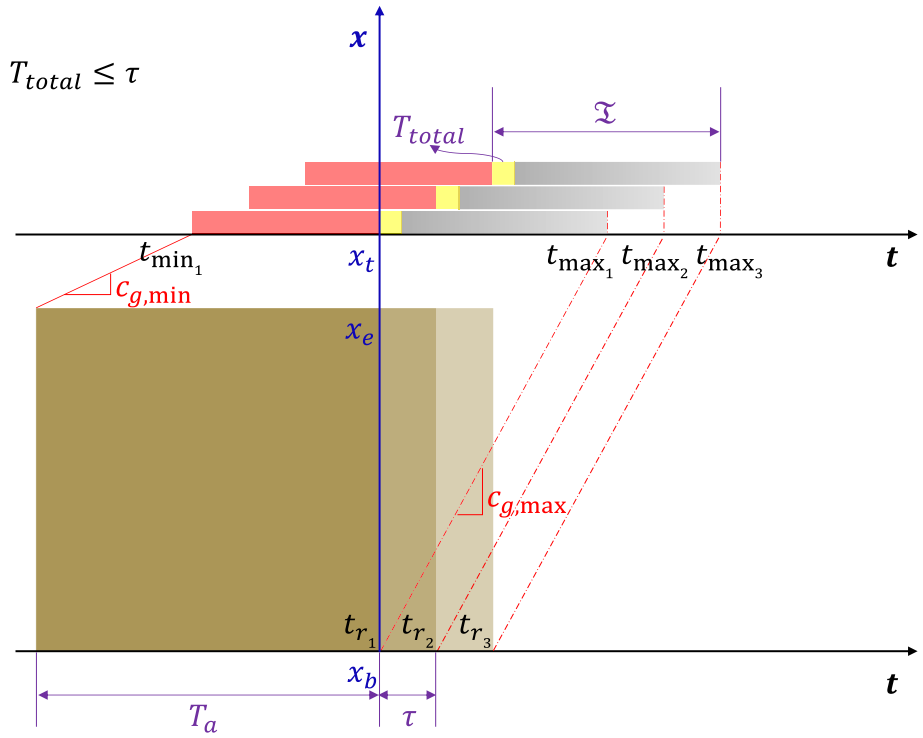

Fig. 2. Overview of how continuous wave prediction is provided by combining a series of short-term deterministic sea wave predictions at x_t based on measurements between x_b and x_e over T_a when $T_{total} \leq \tau$ (——: line with slope $c_{g,\min}$; – – –: line with slope $c_{g,\max}$; gold rectangle: assimilated data; red shading: reconstruction over $t \in [t_{\min}, t_r]$; yellow shading: computation over $t \in [t_r, t_r + T_{total}]$; gray shading: useful prediction zone over $t \in [t_r + T_{total}, t_{\max}]$).

gold rectangles, shifted in time by τ, represent sets of spatio-temporal wave measurements. Here, t_{r_i} corresponds to the latest time used in wave reconstruction for the ith surface sample. At the top of the figures, we present an illustration demonstrating the generation of a continuous time series from a series of color bars. The continuous prediction relies on the useful prediction zone, indicated by the gray shading. To ensure higher prediction accuracy of the continuous wave time series, it is reasonable to select the overlapping waves from subsequent samples. Further, it is given that increased sequence overlap leads to more accurate predictions. It is also possible to use the overlapping waves to quantify the uncertainty of the predicted phase-resolved wave information.

2.3.3. Constraints in continuous wave prediction

When continuously predicting the ocean wave surface on the basis of short-term prediction segments, it becomes evident that the temporal constraints are a balance between various components in time (i.e., T_{total}, τ, and $\mathfrak{T}$). Given the spatio-temporal wave measurement during T_a at the fixed multiple measurement points and the wave spectrum, $\mathfrak{T}$ is likely to remain constant. Thus, we express the constraints of T_{total} and τ as a function of $\mathfrak{T}$. The long-term forecast always starts at the time of completing the first computation (e.g., $t = t_{r_1} + T_{total}$).

In the first case, where $T_{total} \leq \tau$ (see Fig. 1), in order to avoid a missing interval from the starting point, the start of the next prediction (i.e., $t_{r_{i+1}} + T_{total} = i\tau + T_{total}$) must occur before the end of the current prediction (i.e., $t_{\max_i} = (i-1)\tau + \mathfrak{T}$), which yields

$$\begin{aligned} &\tau + T_{total} \leq \mathfrak{T} \\ &\tau \leq \frac{\mathfrak{T}}{2}; \text{ if } T_{total} = \tau. \end{aligned} \tag{11}$$

The actual computation proceeds by means of the discrete data. For the discrete data, the number of points in the short-term forecast used to construct the continuous prediction is $\lceil \frac{\tau}{\Delta t} \rceil$ (where $\lceil\ \rceil$ denotes the least integer function, and Δt is the time step of wave observations).

Unlike the aforementioned case with $T_{total} \leq \tau$, in most multidirectional simulations by nonlinear models, the computation time is longer than the time interval between datasets (i.e., $T_{total} > \tau$, see Fig. 3). These simulations can be further divided into two groups depending on whether multiple processing units or a single processing unit is used. In a computing system with multiple units, two or more processing units are involved in the computations, and thus those different processing units can complete individual computations simultaneously. Therefore, in the case with multiple processing units, as depicted in Fig. 3(a), the short-term forecast can be generated at each τ interval due to wave observations sampled every τ.

When using a single processing unit, the next task will not start until the present process is completed. Thus, T_{total} longer than τ imposes a constraint on the interval between the two short-term forecasts. This results in fewer overlaps between successive sequences compared to the multiple processing units scenario shown in Fig. 3. Consequently, the prediction accuracy of a single processing unit generally deteriorates compared to that of multiple processing units. Note that the number of points selected from each sequence for continuous prediction is $\lceil \frac{\tau}{\Delta t} \rceil$ for multiple processing units and $\lceil \frac{T_{total}}{\Delta t} \rceil$ for a single processing unit. In the scenario with multiple processing units, the number of processing units required to compute the continuous ocean surface is $\lceil \frac{T_{total}}{\tau} \rceil$.

For continuous prediction without any missing points, considering the case of $T_{total} > \tau$ with multiple processing units, the same constraints as in the first case must be satisfied (Eq. (11) or $T_{total} \leq \mathfrak{T} - \tau$). However, in the scenario with a single processing unit, there is a different and more demanding constraint on T_{total}. The beginning of the next useful prediction zone (i.e., $t_{r_{i+1}} + T_{total} = (i+1)T_{total}$) must come before the end of the present one (i.e., $t_{\max_i} = (i-1)T_{total} + \mathfrak{T}$):

$$T_{total} \leq \frac{\mathfrak{T}}{2} \tag{12}$$

2.3.4. Effect of computation time

The effect of T_{total} on continuous wave prediction is discussed in this section. We restrict our attention to the more realistic case of

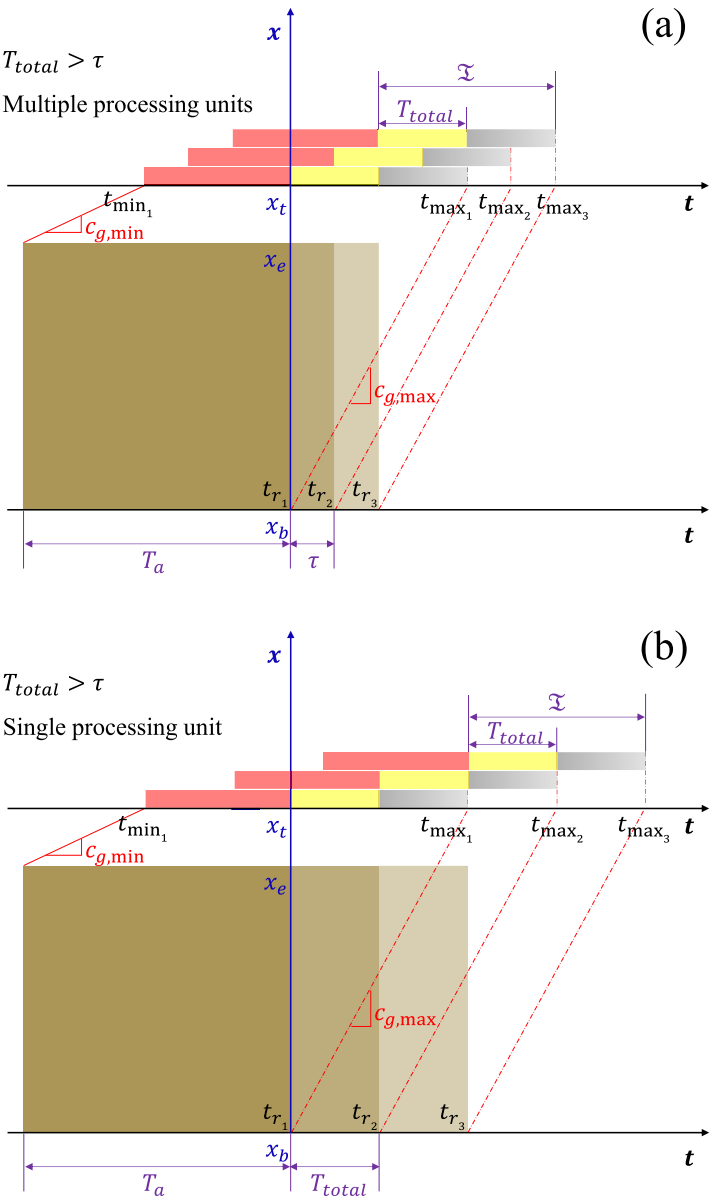

Fig. 3. Configurations of continuous wave prediction depending on the number of processing units, provided at x_t based on measurements between x_b and x_e over T_a when $T_{total} > \tau$: (a) multiple processing units; (b) a single processing unit (——: line with slope $c_{g,\min}$; – – –: line with slope $c_{g,\max}$; gold rectangle: assimilated data; red shading: reconstruction over $t \in [t_{\min}, t_r]$; yellow shading: computation over $t \in [t_r, t_r + T_{total}]$; gray shading: useful prediction zone over $t \in [t_r + T_{total}, t_{\max}]$).

$T_{total} > \tau$ with a single processing unit, and extension to other cases is straightforward. In our design method, the interval used for the continuous wave forecast spans $t' \in [T_{total}, 2T_{total}]$; therefore, T_{total} determines both the starting point and the segment length. When there is a minor difference between the numerical results, particularly near the beginning of the practical prediction zone (i.e., $t' = 0$ or $t = t_r$), a central problem in the study of continuous real-time wave prediction is minimizing T_{total}. Moreover, the temporal evolution of the prediction error across the practical prediction zone by ICWM is more significant than the difference between linear and nonlinear models (Guérin et al., 2019).

Fig. 4 illustrates the effect of T_{total} on model performance for continuous wave prediction. To specifically focus on the influence of T_{total}, we assume the same temporal evolution of errors (i.e., the equivalent gray-scale spectrum). According to Kim et al. (2023), the length of the practical prediction zone under their experimental and numerical setup is about $\mathfrak{T} = 2T_p$. As a reminder, the reconstruction and computation periods, indicated by the red and yellow shadings, respectively, are not available to generate continuous wave prediction. Thus, the continuous forecast always starts at $t = t_{r_1} + T_{total}$. Within the useful prediction zone of each short-term wave prediction (i.e., $t' \in [T_{total}, \mathfrak{T}]$), the purple rectangles indicate the interval used for continuous wave prediction (i.e., $t' \in [T_{total}, 2T_{total}]$). To provide wave prediction continuously without any missing gaps between the short-term intervals, the purple rectangle must remain within the prediction zone, namely, $2T_{total} \le \mathfrak{T}$, which can be rewritten as Eq. (12).

In the first case with $T_{total} < \frac{\mathfrak{T}}{2}$ where overlapping waves exist as shown in Fig. 4(a), we can utilize the second segment instead of relying on the existing forecast when the next forecast becomes available (i.e., $t = t_{r_1} + 2T_{total} = t_{r_2} + T_{total}$). Fig. 4(b) represents the condition with $T_{total} = \frac{\mathfrak{T}}{2}$, and all the short-term forecasts entirely cover the entire time interval but without overlaps. By comparing the continuous time series in Fig. 4(a) and (b), it is evident that the prediction error worsens as T_{total} increases. Furthermore, if T_{total} continues to increase beyond $\frac{\mathfrak{T}}{2}$, a failure occurs in the real-time forecast system due to the missing intervals between forecasts, which visualizes the constraint on T_{total} in Eq. (12).

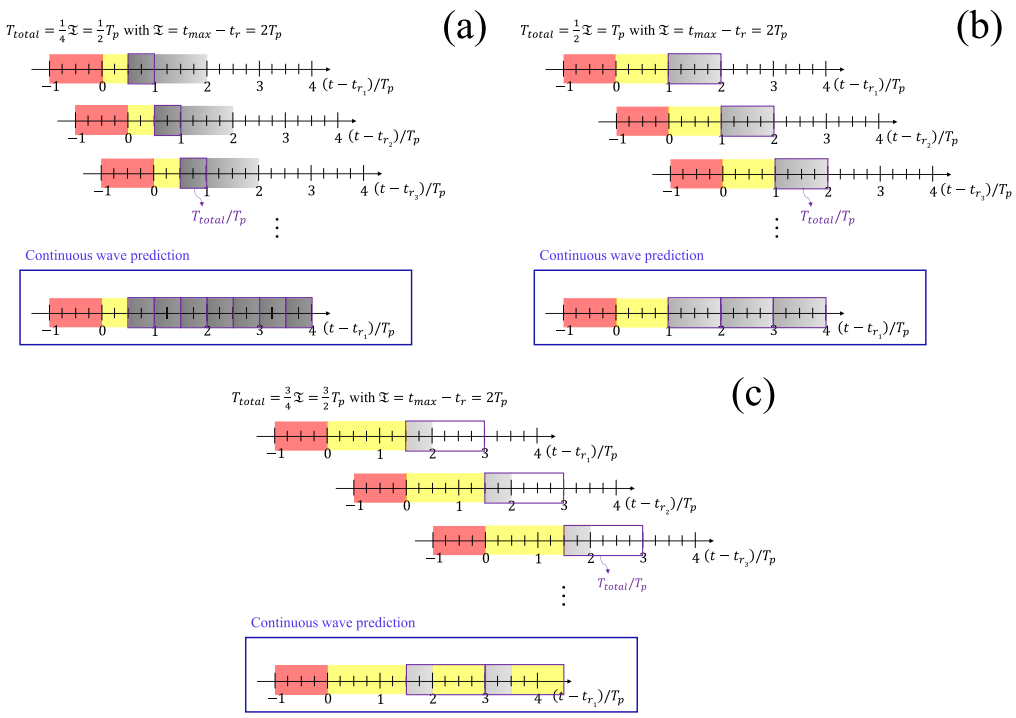

Fig. 4. Effect of T_{total} on continuous wave predictions with a single processing unit when $T_{total} > \tau$ and $\mathfrak{T} = 2T_p$: (a) $T_{total} = \frac{1}{4}\mathfrak{T}$; (b) $T_{total} = \frac{1}{2}\mathfrak{T}$; (c) $T_{total} = \frac{3}{4}\mathfrak{T}$ (purple rectangles encompass the interval used for continuous wave prediction; red shading: reconstruction over $t' = t - t_r < 0$; yellow shading: computation over $t' \in [0, T_{total}]$; gray shading: useful prediction zone over $t' \in [T_{total}, \mathfrak{T}]$).

3. Experimental data

3.1. Setup description

Within the framework of the FLOATECH project, we obtained experimental data in the hydrodynamic and ocean engineering tank, which is 30 m wide, 50 m long, and 5 m deep, at École Centrale de Nantes (ECN) (Bonnefoy et al., 2023). The main purpose of these experiments is to examine the wave model performance for multidirectional and unidirectional nonlinear wave fields toward the location of a floating wind turbine. The absence of the floating structure in the experiments to obtain the measured wave field should be considered as an idealized configuration. In a real (operational) condition, the diffracted and radiated waves from the structure will be measured simultaneously with the incident wave field. This source of uncertainty is not addressed in the present work. However, those waves will propagate away from the structure, and the prediction methodology can solve for different directional components. An adequate methodology could thus be developed to remove the part of the wave field propagating away from the platform in the wave-structure interaction model.

Furthermore, in the present application case, the structure considered is a SPAR platform, the geometry of which can be found in Leroy et al. (2022). At full scale, it exhibits a diameter at the water line of 11.2 m (18 m below the tapper) and a draft of 90 m. In the sea states under consideration, a linear diffraction/radiation computation (Kurnia and Ducrozet, 2023) provides an estimate of the magnitude of this wave field at the measurement location in the range of 5% to 15% of the incident wave field (decreasing rapidly with distance from the platform).

With a wavemaker at one end and an absorbing beach at the other extremity, irregular wave fields were generated using a Pierson-Moskowitz spectrum (Pierson and Moskowitz, 1964) with the peak period $T_p = 12$ s at full scale, and at the geometric scale of 1:40 (1: $\sqrt{40}$ Froude scaling for time). The experiments are inherently nonlinear because water with a free surface is, in general, a nonlinear medium. To investigate the effects of the extent of nonlinearity on ocean wave

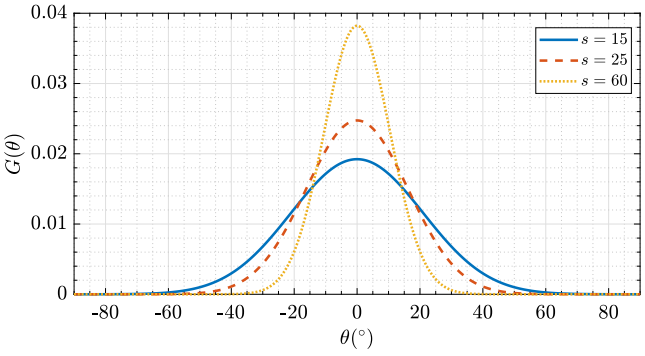

Fig. 5. Directional spreading for multidirectional cases where s is the spreading factor of the angular spreading function (——: $s = 15$; − − −: $s = 25$; ·····: $s = 60$).

prediction, different significant wave heights H_s or the corresponding characteristic wave steepnesses H_s/L_p are considered. A range of wave steepnesses is represented from 2.2% to 4%, in deep water with $k_p d \approx 5.6$ (Dean and Dalrymple, 1991), where k_p and d denotes the peak wavenumber and water depth, respectively. The peak wavelength is $L_p = 225$ m which is equivalent to 5.62 m at the tank scale. Moreover, for a more comprehensive study of directional wave sea states, we consider three different directional spreading values in multidirectional waves, but with a moderate nonlinearity $H_s/L_p = 3.1\%$ (see Fig. 5).

Table 1 summarizes the experimental setup for all the cases. To obtain multidirectional wave fields, the spectrum in frequency is multiplied by the angular spreading function with the spreading factor s in Mitsuyasu et al. (1975):

$$G(\theta) = \frac{2^{2s-1}}{180}\frac{(s!)^2}{(2s)!}\cos^{2s}\left(\frac{\theta}{2}\right) \text{ for } \theta \in [-180°, 180°] \tag{13}$$

where the main propagation direction is 0°.

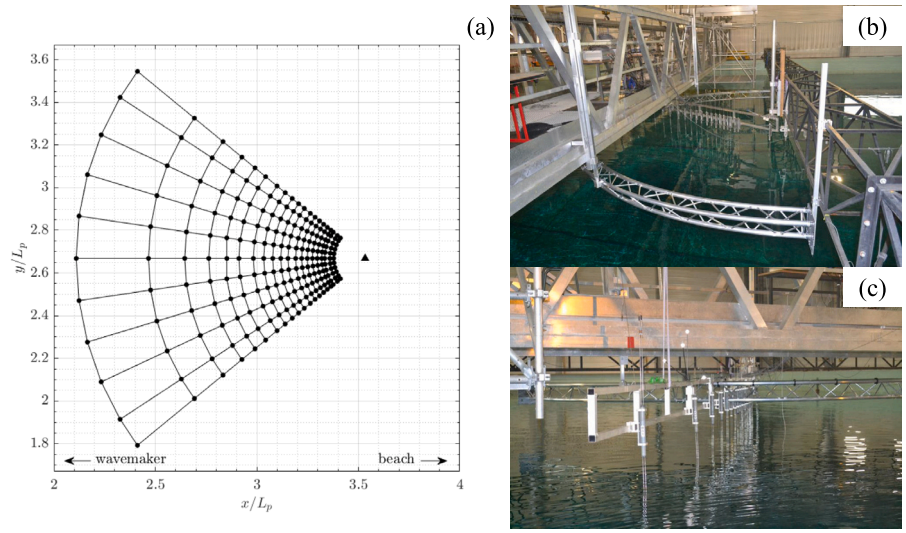

Fig. 6. (a) Location of wave gauges; (b, c) wave gauges mounted on rotating structure (•: wave observations; ▲: location of turbine, WG21).

Table 1
Wave information and setup of experiments.

Case	H_s (m)	H_s/L_p (%)	s	J_θ
A	7	3.1	15	11
B	7	3.1	25	9
C	7	3.1	60	7
D	5	2.2	25	9
E	9	4.0	25	9

To mimic a network of wave measurements, denoted as $J_r \times J_\theta$ rays on the mean free surface (where J_r is the total number of wave gauges installed on a straight structure and J_θ is the total number of directional arrays for the measurement zone, see Fig. 6), as captured by the optical system, we used a straight rotating structure with 20 wave gauges (i.e., $J_r = 20$). Thanks to the rotating structure and the repeatability of the experiments, we obtained directional measurements on the $J_r \times J_\theta$ grid. Repeatability errors of the multidirectional cases have been assessed using reference wave gauges. It is evaluated on the significant wave height with a 3% variation, or 0.24 m at full scale (Kim et al., 2023). Although this measurement variation induced by repeated measurements is likely to increase the prediction error for multidirectional sea states, Kim et al. (2023) achieved comparable model accuracy in both multidirectional and unidirectional cases. The latter did not involve any repeatability. The assimilation procedure is performed based on discrete wave gauges rather than continuous data collection in the spatial domain. An additional downstream wave gauge WG21 (or target location) was installed about $0.15L_p$ away from the end of the measurement area. The temporal extent of wave data used in the present study is limited by $t_b - t_a \approx 506T_p$ with $t_a/T_p \approx 158$ to ensure that all the wave components generated by the wavemaker had reached the entire domain of the tank. Also, the end of the time series measured in experiments was used for that in this study $t_b/T_p \approx 664$ because the wave measurements were taken up until the point at which the wavemaker was stopped. For details on the experiments, the reader is referred to Kim et al. (2023).

3.2. Prediction zone

As stated earlier, the short-term wave forecast is valid within the prediction zone that is determined by the group velocities and the propagation directions of wave components. Kim et al. (2023) specified the three-dimensional spatio-temporal prediction zone based on the spatial sampling of the wave field (see Fig. 6) over the assimilation time T_a. The frequency range therein was determined by the upper and lower cutoff limits using a small fraction of the wave spectrum at the peak frequency f_p with $\mu = 0.05$:

$$S_\eta(\omega_{\min}) = S_\eta(\omega_{\max}) = \mu S_\eta(\omega_p) \tag{14}$$

where $S_\eta(\omega)$ refers to the power spectral density.

The prediction zone was derived based on the identical directional bandwidth $[\theta_{\min}, \theta_{\max}] = [-\theta_{\lim}, \theta_{\lim}]$ with $\theta_{\lim} = 45°$ for all the multidirectional cases irrespective of the directional spread. However, this directional range with $\theta_{\lim} = 45°$ is likely to be a conservative setting in a sea state with a relatively small directional spreading (e.g., $s = 60$ in Fig. 5), increasing the numerical cost unnecessarily in both the nowcast and forecast steps owing to the excessive number of wave components. In practice, the wave fields captured by a structure-mounted optical sensor may have to be restricted to a narrower direction range when they arrive at the floating offshore wind turbine. To this effect, it is desirable to optimize the direction domain fit for each wave condition, and then the prediction zone suggested by Kim et al. (2023) should be generalized to consider different direction bandwidths with respect to the directional limit (i.e., $\theta_{\lim}$).

In Fig. 7, the reconstruction and prediction zones are indicated by the red and gray shadings, respectively. For simplicity, based on the observation zone provided by a matrix of $J_r \times J_\theta$ in Fig. 6(a), the reconstruction zone is approximated with the boundaries consisting of a selected few points (i.e., polygon $ABDFGH$ in Fig. 7(a)). Point A corresponds to the intersection point between the left boundary propagating in the direction of $-\theta_{\lim}$ and the right boundary propagating in the direction of $\theta_{\lim}$ (i.e., $x = \tan(\theta_{\lim})(y' - y'_B) + x_B$ and $x = -\tan(\theta_{\lim}) + x_H$, respectively, where $y' = y - y_c$ denotes the relative y-coordinate with respect to the centerline $y = y_c$). Points B, D, F, and H are the selected observation points, and point G is a reflected point of point A over $y' = 0$.

During the data assimilation step with the assimilation time T_a, the prediction zone is extended by an advance of the right boundary, as shown in Fig. 7(b). Specifically, the right boundary propagates over a time interval of T_a with the speed of $c_{g,\min}$ in the direction of θ, or alternatively, with the speed of $c_{g,\min}/\cos(\theta)$ in the $+x$ direction. From the end of the assimilation procedure (i.e., $t = t_r$), as the reconstructed wave fields propagate in time and space, the accessible prediction zone starts to transform and eventually disappears, which implies that the wave measurements become obsolete and no longer able to provide wave forecast. For details on the algorithms of developing the directional prediction zone, the reader is referred to Qi et al. (2018b) and Kim et al. (2023). This temporal evolution of the prediction zone

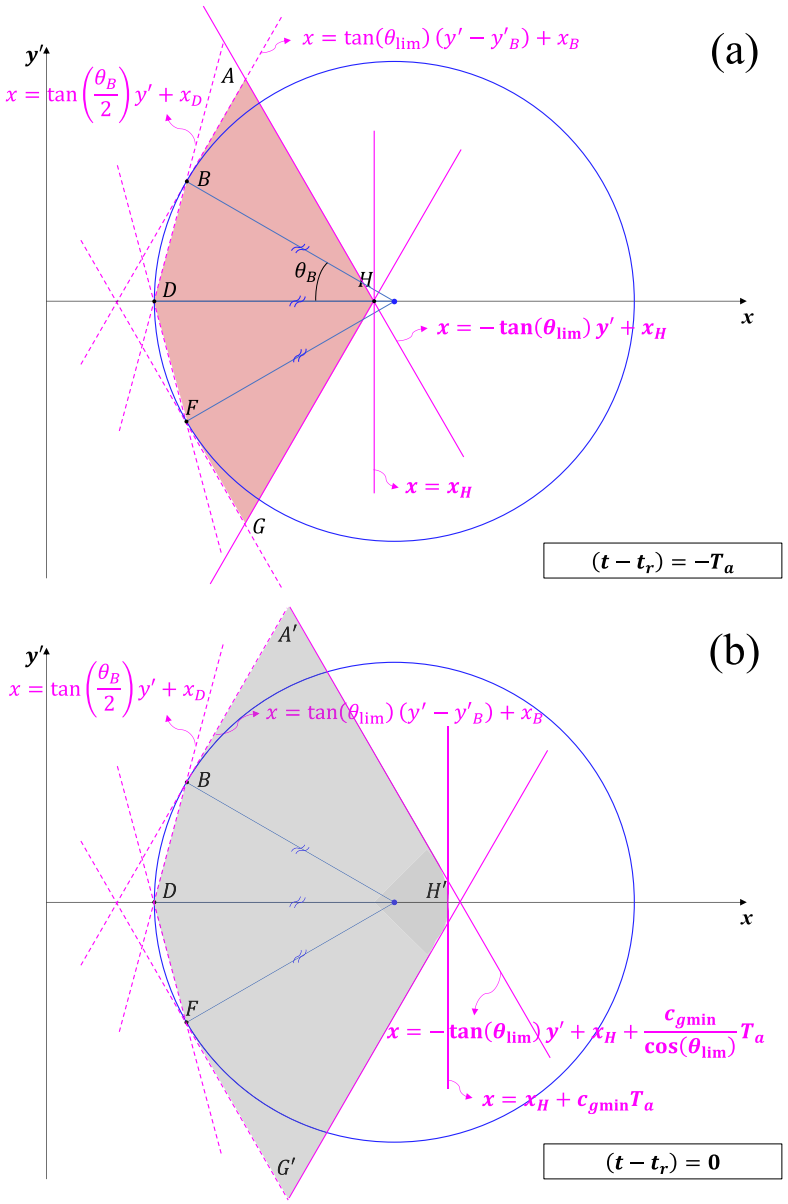

Fig. 7. Reconstruction and prediction zones: (a) reconstruction zone at $(t - t_r) = -T_a$; (b) prediction zone at $(t - t_r) = 0$ (– – : left boundary; ——: right boundary; red shading: nowcast; gray shading: forecast).

is divided into two types according to whether $\theta_{\lim}$ is larger or smaller than a quarter of the horizontal aperture angle $\frac{\theta_B}{2} = \frac{\beta_a}{4}$.

First, when $\theta_{\lim} \geq \frac{\theta_B}{2}$, since the direction of wave components influences the x-component of the corresponding group velocity, the lines of $\pm\theta_{\lim}$ and $\pm\frac{\theta_B}{2}$ together describe the left boundary of the prediction zone. On the other hand, all the prespecified wave components in the direction work in concert to give the right boundary a fan-shape (Qi et al., 2018b):

$$\max\begin{bmatrix} \tan(\theta_{\lim})(y' - y'_B) + x_B + \frac{c_{g,\max}}{\cos(\theta_{\lim})} t', \\ -\tan(\theta_{\lim})(y' - y'_F) + x_F + \frac{c_{g,\max}}{\cos(\theta_{\lim})} t', \\ \pm\tan\frac{\theta_B}{2} y' + x_D + \frac{c_{g,\max}}{\cos(\theta_B/2)} t' \end{bmatrix} \leq x \leq \min_{\theta\in[-\theta_{\lim},\theta_{\lim}]} \begin{bmatrix} -\tan\theta y' + x_H \\ +\frac{c_{g,\min}(T_a + t')}{\cos\theta} \end{bmatrix} \tag{15}$$

where $y' = y - y_c$ and $t' = t - t_r$. If the targeted point along the centerline $y' = 0$ falls inside an allowable range (i.e., $x < x_H + c_{g,\min} T_a$), Eq. (15) can be reduced to the practical prediction zone $t' \in [0, t'_{\max}]$:

$$t'_{\max} = \min\left[\frac{x - x_D}{c_{g\,\max}}\cos(\theta_B/2), \frac{x - x_B + \tan(\theta_{\lim}) y'_B}{c_{g\,\max}}\cos(\theta_{\lim})\right] \tag{16}$$

The practical prediction zone must be distinguished from the prediction zone in the previous studies (Desmars et al. 2020, Kim et al. 2023).

Secondly, it is probably sufficient to provide wave simulations with $\theta_{\lim}$ smaller than $\frac{\theta_B}{2}$ in the multidirectional case with very small directional spreading (cf. $\theta_{\lim} = 0°$ in the unidirectional case). As the lines of $\pm\theta_{\lim}$ move faster than those of $\pm\theta_{\lim}$ in the $+x$-direction, the lines of $\pm\theta_{\lim}$ determine the left boundary. Accordingly, Eq. (15) is simplified to Eq. (17):

$$\max\begin{bmatrix} \tan(\theta_{\lim})(y' - y'_B) + x_B + \frac{c_{g,\max}}{\cos(\theta_{\lim})} t', \\ -\tan(\theta_{\lim})(y' - y'_F) + x_F + \frac{c_{g,\max}}{\cos(\theta_{\lim})} t' \end{bmatrix} \leq x \leq \min_{\theta\in[-\theta_{\lim},\theta_{\lim}]} \begin{bmatrix} -\tan\theta y' + x_H \\ +\frac{c_{g,\min}(T_a + t')}{\cos\theta} \end{bmatrix} \tag{17}$$

which yields the practical prediction zone $t' \in [0, t'_{\max}]$ in the case of $\theta_{\lim} < \frac{\theta_B}{2}$:

$$t'_{\max} = \frac{x - x_B + \tan(\theta_{\lim}) y'_B}{c_{g\max}} \cos(\theta_{\lim}) \tag{18}$$

Notably, as the direction bandwidth considered is narrower with the smaller $\theta_{\lim}$, the practical prediction zone is extended due to the increasing $t'_{\max}$, although the change is not significant.

4. Strategies for continuous wave prediction

The previous numerical modeling setups in Kim et al. (2023) were optimized for short-term wave prediction over the prediction zone $t \in [t_{\min}, t_{\max}]$. It is necessary, therefore, to modify the wave setups for continuous wave prediction. We also examine the modification to the iterative process proposed in Section 2.2.2.

One unbiased measure of the error in the wave prediction is an ensemble average of the normalized misfit error over a great number of surface samples which partly overlap each other with a shifting time τ. The surface samples, each comprising one nowcast (or assimilation) and one forecast (or prediction), were generated from a single sea state over a sufficiently long time, and N_s samples were then used to compute the normalized misfit error:

$$\varepsilon(x, y, t) = \frac{1}{N_s} \sum_{i=1}^{N_s} \frac{\left| \eta_{pred,i}(x, y, t) - \eta_{ref,i}(x, y, t) \right|}{H_s} \tag{19}$$

where $\eta_{pred,i}$ and $\eta_{ref,i}$ denote the predicted and observed ocean surface of the ith sample, respectively. Following Kim et al. (2023), $N_s = 400$ with $\tau/T_p = \Delta t/T_p = 0.053$ was employed since it led to an efficient convergence in the prediction error.

Assuming $\tau = \Delta t \approx 0.6$ s at a full-scale is considered acceptable since the sampling time of wave observation data is on the order of 1 s (e.g., Zhang et al. 2022a, Lee et al. 2022). Furthermore, the model of LWT is fast enough to complete the simulation within Δt. Therefore, assuming $\tau > \Delta t$ would likely be detrimental to the linear wave model. As discussed in Section 2.3.3, τ determines the number of points in the short-term forecast used for the continuous time series. It is hence more disadvantageous for LWT to utilize more points under the assumption of a larger τ, as nonlinear wave effects play an increasingly large role over time. In other words, setting $\tau = \Delta t$ may be the optimal condition to showcase the effect of the strategies on the prediction accuracy of continuous prediction by ICWM.

Aiming at providing a continuous prediction based on the practical prediction zone $t \in [t_r, t_{\max}]$, the averaged misfit error is obtained over the practical prediction zone:

$$\varepsilon^{PP}(x, y) = \frac{1}{t_{\max} - t_r} \int_{t_r}^{t_{\max}} \varepsilon(x, y, t)\, dt \tag{20}$$

To evaluate the overall continuous wave prediction, the normalized misfit error between the prediction surface elevations η_{pred} and the reference ones η_{ref} is averaged over the entire duration from t_a to t_b:

$$\varepsilon^{CP}(x, y) = \frac{1}{t_b - t_a} \int_{t_a}^{t_b} \frac{|\eta_{pred}(x, y, t) - \eta_{ref}(x, y, t)|}{H_s} dt \tag{21}$$

The improved surface similarity parameter (ISSP), introduced by Kim et al. (2023), assesses prediction values with consideration of the deviation from the frequency-averaged reference value $\overline{F}_{\eta,ref}$. In contrast, when using the surface similarity parameter (SSP, Perlin and Bustamante 2016), an overestimated value would be considered more highly than an underestimated one. We calculate the ISSP value over the entire experimental duration:

$$ISSP = \frac{\left(\int \left| F_{\eta,pred}(f) - F_{\eta,ref}(f) \right|^2 df \right)^{1/2}}{\left(\int \left[\left| F_{\eta,pred}(f) - \overline{F}_{\eta,ref} \right| + \left| F_{\eta,ref}(f) - \overline{F}_{\eta,ref} \right| \right]^2 df \right)^{1/2}} \tag{22}$$

where $F_{\eta,pred}$ and $F_{\eta,ref}$ refer to Fourier transforms of prediction and reference surface elevations, respectively.

Table 2
Directional cutoff and the number of directional components.

Case	$\theta_{\lim}$ (°)	$N_\theta^{Present}$	$N_\theta^{Previous}$	H_s/L_p (%)	s
A	35	5	9	3.1	15
B	35	5	7	3.1	25
C	25	3	5	3.1	60
D	35	5	9	2.2	25
E	35	5	7	4.0	25

4.1. Wave parameters for prediction

The short-term deterministic wave prediction algorithms require a relevant size of wave observations in time and space. As in Kim et al. (2023), the total number of spatio-temporal data used in the data assimilation was $L = J \times K = J_r \times J_\theta \times K = 20 \times J_\theta \times 100$ (J_θ is given in Table 1), where $K = 100$ was found to achieve a balance between model accuracy and numerical efficiency.

To link the wave fields used in the algorithms and the spatial coverage of the optical sensor, the wave prediction is based on a different frequency domain from the one used for the prediction zone in Eq. (14). As in the previous studies, the wavenumber of the last frequency component k_{N_ω} is specified in advance by a multiple of the peak wavenumber k_p via the linear proportional relationship between k_{N_ω} and N_ω (i.e., $k_{N_\omega} = \frac{2N_\omega}{5} k_p$). The wavenumber of the first component is then obtained by combining the spatial sampling of wave measurements and the advection of wave information during T_a:

$$k_1 = \frac{2\pi}{x_e - x_b + c_{g,N_\omega} T_a} \tag{23}$$

where unlike the beginning point along the centerline x_b, the end point x_e depends on the spreading factor s and hence, J_θ. The group velocity of the last component c_{g,N_ω} is given by the deep water dispersion relationship ($c_{g,N_\omega} = \frac{1}{2}\sqrt{g/k_{N_\omega}}$). For the direction domain in the numerical framework, the same direction cutoff with $\theta_{\lim}$ as in the prediction zone is selected. More details in bandwidths such as conditions for the unique solution are discussed in detail in Kim et al. (2023).

4.2. Direction cutoff

Kim et al. (2023) employed the same directional domain with $\theta_{\lim} = 45°$ irrespective of the directional spreading in all the multidirectional cases. However, it is probably too wide for the small directional spreading case. It is, therefore, necessary to optimize $\theta_{\lim}$ and the corresponding N_θ for each case, which is expected to contribute to faster computation. By considering a narrower direction bandwidth with different values of $\theta_{\lim}$, the analysis of the misfit error with increasing N_θ was carried out to gain insight into the relevant direction cutoff and its physical characteristics. Here, we consider the minimum of the practical prediction zones of all the $\theta_{\lim}$ (i.e., $\theta_{\lim} = 45°$) in calculating ε^{pp} in order to use the identical horizon and to fall inside the prediction zone.

We note that relatively high performances are achieved with $N = 3$ and $\theta_{\lim} = 15°$, demonstrating (1) almost no influence of $\theta_{\lim}$ when using the minimum number of directional components (i.e., $N_\theta = 3$) to model the large directional spreading case (i.e., Case A), (2) poor results when using $N_\theta = 3$ with large $\theta_{\lim}$ in the case of small directional spreading case (e.g., Case C) due to excessively wide bandwidths, and (3) a counterproductive effect arising from an excessive number of components when $\theta_{\lim} = 15°$. In addition, the previous numerical setup in direction is confirmed to be extremely wide as the smaller $\theta_{\lim}$ and N_θ give almost the same results as the previous $\theta_{\lim} = 45°$ and N_θ in most cases (see Fig. 8 and Table 2). The results in Cases D and E are not shown here for the sake of simplicity; the summary of optimal direction bandwidths in all the cases is presented in Table 2.

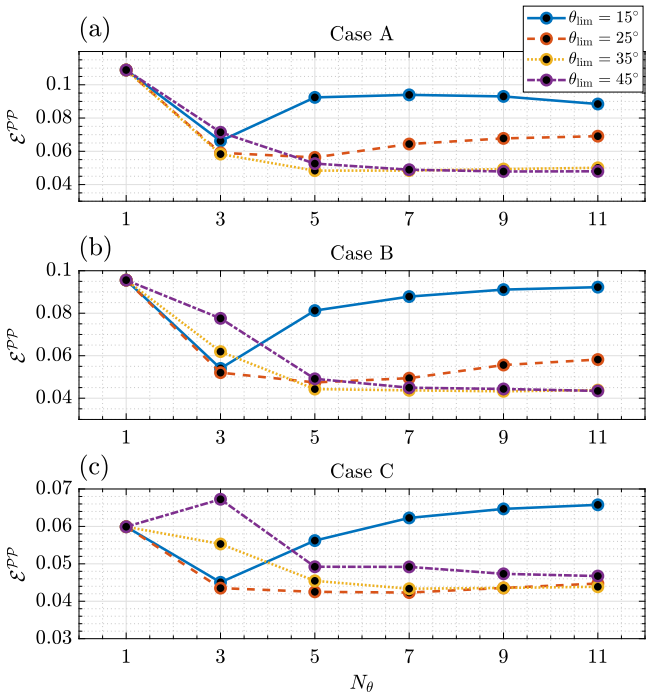

Fig. 8. Averaged misfit error of surface elevation over the practical prediction zone by ICWM at WG21 against N_θ and $\theta_{\lim}$: (a) Case A; (b) Case B; (c) Case C (——: $\theta_{\lim} = 15°$; – – ·: $\theta_{\lim} = 25°$; ·····: $\theta_{\lim} = 35°$; —·—: $\theta_{\lim} = 45°$).

Table 3
Energy contents depending on the directional spread and direction cutoff where the optimized condition is highlighted in bold.

s	$\theta_{\lim} = 15°$	$\theta_{\lim} = 25°$	$\theta_{\lim} = 35°$	$\theta_{\lim} = 45°$
15	53.2%	77.5%	**91.1%**	97.2%
25	65.0%	88.1%	**97.2%**	99.5%
60	85.1%	**98.4%**	100%	100%

It is surprising that the modified direction domain even captures the properties of the wave field evolution more accurately in Case C, which features the smallest directional spread. It appears that a better understanding of wave prediction is achieved by excluding the unnecessary components of the wide angles because this can definitely eliminate the possibility of containing the energy of the large-angle components. Fig. 9(a), (b), and (c) show how the ratio of the present direction bandwidth to the previous one changes in time and space, and Fig. 9(d) illustrates the temporal evolution of the ratio at the point of interest (WG21). The modification to the direction cutoff and the corresponding value of N_θ improved the prediction accuracy, especially around the target point. As time increases over the practical prediction zone, the modified direction setup consistently improves the accuracy of phase-resolved wave propagation, particularly around the target point.

Table 3 and Fig. 10 provide insight and guidance into the suitable direction limit linked to the directional spread of each case, where the optimized condition selected is highlighted in bold. It is suggested that the direction bandwidth should contain at least 90% of the energy to appropriately understand the short-crested waves. Moreover, employing an excessively wide direction domain may have a counterproductive effect on deterministic wave prediction (i.e., $\theta_{\lim} = 45°$ in Case C with $s = 60$).

4.3. Frequency cutoff

We should also optimize the frequency domain in the form of the frequency cutoff k_{N_ω} and the number of the frequency components N_ω for continuous wave forecasting. In their study, Kim et al. (2023) found that setting $k_{N_\omega} = 12k_p$ with $N_\omega = 30$ minimized the averaged misfit error throughout the prediction zone $t \in [t_{\min}, t_{\max}]$ at the target position. However, for the purpose of continuous wave forecasting, it is more relevant to focus on the initial part of the practical prediction zone rather than on the entire prediction zone.

Fig. 11 shows the temporal evolution of the misfit error against N_ω when the modified direction domain is applied. Although N_ω appears to have a very limited effect on the prediction error in Case A, $N_\omega = 30$ better describes the overall prediction of the wave propagating in Cases B and C compared to $N_\omega = 20$. However, the beginning of the practical prediction zone around $t = t_r$ is not noticeably influenced by N_ω. This suggests that $N_\omega = 30$ was selected in the study for short-term prediction due to the extended prediction zone in time rather than the lower prediction errors across the entire time horizon. Therefore, a decrease in N_ω can be preferred as long as it reduces the computational demands and has a negligible effect on the error evolution over the segment $t' \in [T_{total}, 2T_{total}]$ employed for continuous forecasting. On the other hand, increasing N_ω beyond $N_\omega = 30$ (i.e., $N_\omega = 40$) confirms that the wavenumber space with $N_\omega = 30$ is sufficient to describe ocean wave propagation, and further increases may induce counterproductive nonlinear effects on the nonlinear wave group velocity c_{g,N_ω} (Qi et al., 2018a).

5. Numerical results

5.1. Numerical efficiency and stability

Tables 4 and 5 show the effect of the strategies on the numerical efficiency and stability in terms of T_{total}, as well as the averaged iteration number and convergence probability of finding the wave amplitude parameters during the nowcast step. The computations were done on an Intel(R) Core(TM) i7-8700 CPU 3.20 GHz. We note that the constraint for continuous wave prediction (i.e., Eq. (12) with $\mathfrak{T} = 2T_p$) is satisfied even with the previous numerical setup of the prediction algorithm in Kim et al. (2023).

With the modification in the iterative process (i.e., initial guess, error tolerance, and maximum iteration number), it is clear from the comparison of the first and second rows that a significant improvement in computational efficiency is achieved. In most cases, a slightly greater convergence probability (or improved numerical stability) is observed, particularly due to the change in the initial guess. In addition, the strategies of employing narrower bandwidths and fewer wave components, both in direction and frequency, ease computational loads. Overall, the strategies designed to perform continuous real-time wave prediction by ICWM reduce the computation time by a factor of about 5 to 13 compared to the previous developments. It should be noted that the entire calculation using LWT, under the optimized numerical condition in terms of N_ω and N_θ, was completed within a time step of wave observations Δt in all cases. The CPU time taken by ICWM under the optimum condition increases with the directional spread (or decreasing s) and wave steepness, as shown in Tables 4 and 5, respectively.

5.2. Continuous wave prediction

With the strategies for continuous wave prediction in the numerical simulation, an ensemble average of the normalized misfit error (i.e., ε) over $N_s = 400$ in Case A was obtained for LWT, LWT-CDR, and ICWM in Fig. 12. To assess the modifications considered for continuous wave prediction, we compare it with the temporal evolution of the prediction error by ICWM using the previous wave components. It should be noted that, for LWT, the continuous time series consists only of a single point from every surface sample due to the fairly short computation time (i.e., $T_{total} < \Delta t$), which is indicated by the single blue point at the beginning of the dash-dotted black line. Regardless of how small T_{total}

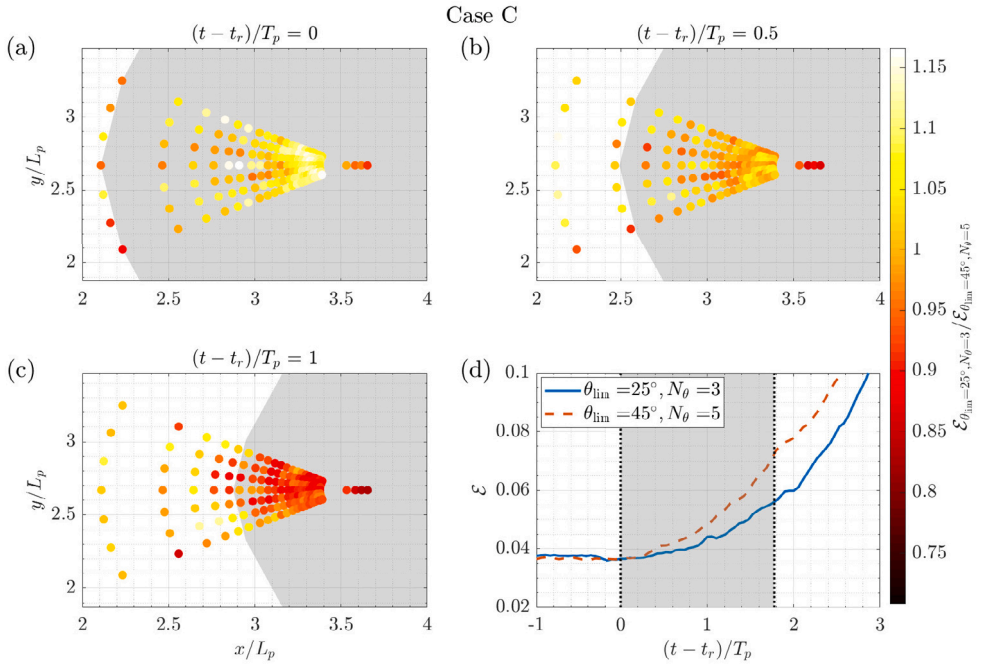

Fig. 9. Comparison of prediction error between the previous and present direction bandwidths for Case C using ICWM: (a) $(t-t_r)/T_p = 0$; (b) $(t-t_r)/T_p = 0.5$; (c) $(t-t_r)/T_p = 1$; (d) temporal evolution at WG21 (filled circles: ratio of prediction error at WGs; gray shading: practical prediction zone; ——: present direction bandwidth; – – ·: previous direction bandwidth; ·····: boundaries of practical prediction zone).

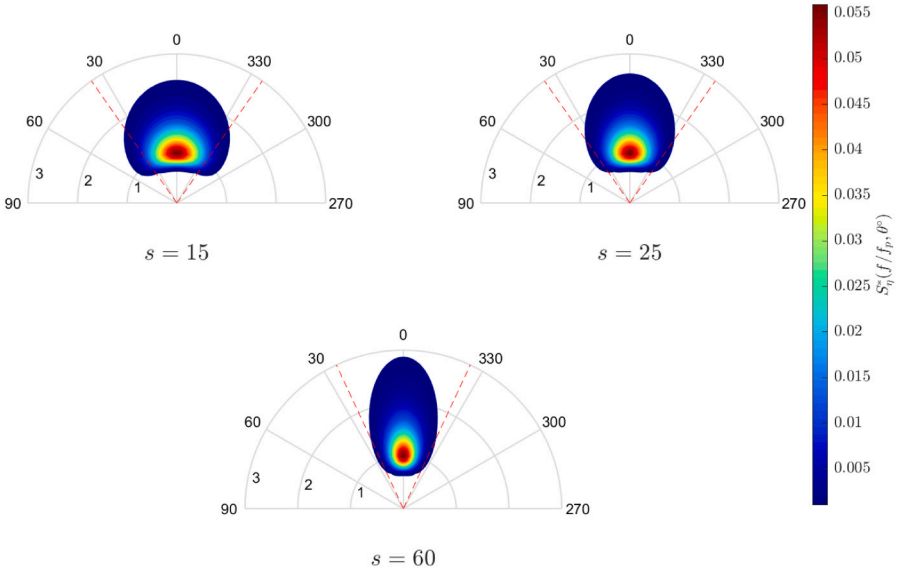

Fig. 10. Normalized spectral density $S_\eta^* = S_\eta f_p/(H_s^2/16)$ and direction cutoff $\theta = \pm\theta_{\mathrm{lim}}$ (– – ·): (a) $s = 15$; (b) $s = 25$; (c) $s = 60$.

is, the prediction at $t = t_r$ is unavailable for constructing the continuous time series.

Compared to the present development of ICWM, the previous ICWM better predicts the reference ocean surfaces toward the end of the prediction zone (see the solid and dashed lines in black in Fig. 12). In contrast, LWT exhibits a greater error than ICWM over the entire prediction zone (see the dash-dotted line in black in Fig. 12). However, when using the previous numerical setup for ICWM, a substantial prediction error is associated with the continuous wave forecast (indicated in blue in Fig. 12) due to the relatively long computation time, as shown in Table 4. By reducing the number of wave components and modifying the frequency and direction cutoffs, ICWM is able to provide a continuous wave forecast interval that falls within the front part of the practical prediction zone, which has lower prediction errors.

As a result, as shown in Fig. 13, ICWM with the previous selection yields a continuous wave prediction that is worse than LWT, while ICWM with the present selection shows improvement. It can be observed that the start point is determined by T_{total} in Tables 4 and 5.

Table 4
Comparison of numerical cost and stability between cases with different directional spreads s where $T_p = 12$ s and $\tau = \Delta t = 0.6$ s at full scale.

$s = 15$ Case A	Previous ICWM	ICWM			LWT-CDR	LWT
$\theta_{\lim}$	45°	45°	35°	35°	35°	35°
$N_\omega \times N_\theta$	30 × 9	30 × 9	30 × 5	20 × 5	20 × 5	20 × 5
T_{total} (s)	7.6	3.5	1.7	1.0	0.7	0.4
Iteration number	5.8	3.1	3.2	3.1	2.9	–
Convergence probability	98.5%	98.3%	96.5%	97.3%	99.8%	–
$s = 25$ Case B	Previous ICWM	ICWM			LWT-CDR	LWT
$\theta_{\lim}$	45°	45°	35°	35°	35°	35°
$N_\omega \times N_\theta$	30 × 7	30 × 7	30 × 5	20 × 5	20 × 5	20 × 5
T_{total} (s)	5.4	2.3	1.5	1.0	0.6	0.3
Iteration number	6.2	3.3	3.4	3.2	2.9	–
Convergence probability	97.0%	97.8%	97.5%	96.5%	100%	–
$s = 60$ Case C	Previous ICWM	ICWM			LWT-CDR	LWT
$\theta_{\lim}$	45°	45°	25°	25°	25°	25°
$N_\omega \times N_\theta$	30 × 5	30 × 5	20 × 3	20 × 3	20 × 3	20 × 3
T_{total} (s)	3.2	1.3	0.8	0.5	0.3	0.2
Iteration number	6.4	3.5	3.7	3.5	3.0	–
Convergence probability	96.5%	97.8%	94.5%	95.3%	99.3%	–

Table 5
Comparison of numerical cost and stability between cases with different wave steepnesses H_s/L_p where $T_p = 12$ s and $\tau = \Delta t = 0.6$ s at full scale.

$H_s/L_p = 2.2\%$ Case D	Previous ICWM	ICWM			LWT-CDR	LWT
$\theta_{\lim}$	45°	45°	35°	35°	35°	35°
$N_\omega \times N_\theta$	30 × 9	30 × 9	30 × 5	20 × 5	20 × 5	20 × 5
T_{total} (s)	8.1	2.6	1.2	0.8	0.5	0.3
Iteration number	5.4	2.8	2.8	2.8	2.8	–
Convergence probability	99.0%	99.3%	98.5%	98.8%	99.5%	–
$H_s/L_p = 3.1\%$ Case B	Previous ICWM	ICWM			LWT-CDR	LWT
$\theta_{\lim}$	45°	45°	35°	35°	35°	35°
$N_\omega \times N_\theta$	30 × 7	30 × 7	30 × 5	20 × 5	20 × 5	20 × 5
T_{total} (s)	5.4	2.3	1.5	1.0	0.6	0.3
Iteration number	6.2	3.3	3.4	3.2	2.9	–
Convergence probability	97.0%	97.8%	97.5%	96.5%	100%	–
$H_s/L_p = 4.0\%$ Case E	Previous ICWM	ICWM			LWT-CDR	LWT
$\theta_{\lim}$	45°	45°	35°	35°	35°	35°
$N_\omega \times N_\theta$	30 × 7	30 × 7	30 × 5	20 × 5	20 × 5	20 × 5
T_{total} (s)	12.8	2.7	1.9	1.0	0.6	0.3
Iteration number	7.4	3.6	4.0	3.6	3.0	–
Convergence probability	96.5%	97.8%	94.5%	95.3%	99.5%	–

The effect of the strategies is most pronounced in Case E, where the greatest wave steepness resulted in the longest T_{total}. To quantitatively assess the continuous wave prediction over the entire duration, we obtained ε^{CP} and ISSP (see Fig. 14). Since the computation of the misfit error in Fig. 12 is based on the early part of the experimental duration (i.e., $N_s = 400$), the errors are higher in Fig. 14. The prediction errors of LWT and LWT-CDR with the new numerical setup fall between those of ICWM with the previous and current setups. Therefore, the strategies used for efficient numerical modeling are valid for providing continuous wave forecasts.

At this stage, it would be opportune to study the effect of wave conditions, including varying directional spreads and wave steepnesses. The better prediction performance by ICWM compared to LWT and LWT-CDR with decreasing directional spreading is consistent with the findings of Kim et al. (2023). As can be visually observed in Fig. 13(e), reducing T_{total} worked best in Case E with the greatest wave steepness, while the performances with or without the strategies become almost equivalent in Case D with the smallest wave steepness. Although a linear description of the ocean surface may be sufficient for the experimental condition investigated in this study, as the time and space scales of the wave field increase, the nonlinear wave properties will become more critical for more precise predictions.

6. Conclusions

Most previous studies on real-time deterministic sea wave prediction have primarily focused on short-term prediction, especially in time. However, in the final stage of a real-time wave prediction system, it is essential to continuously describe the ocean surface using short-term predictions. Therefore, we develop algorithms for continuous wave prediction in time, especially for directional sea states, involving a novel study on a couple of significant time components considered in an operational scenario for real-time wave prediction. These include the update interval of the wave datasets τ and the total calculation time T_{total}. Also, the length of the practical prediction zone $\mathfrak{T}$ is given by both the distance from the observation zone to the point of interest and the maximum group velocity of the prescribed wave spectrum.

In their study, Kim et al. (2023) optimized wave parameters within the prediction zone $t' \in [-T_a, \mathfrak{T}]$, which encompasses reconstructed waves over $t' \in [-T_a, 0]$ and predicted waves over $t' \in [0, \mathfrak{T}]$. However, when providing continuous wave predictions, the wave reconstruction and the wave prediction over $t' \in [0, T_{total}]$ are not available. In light of this, we use the terms "practical prediction zone" and "useful prediction zone" to denote the shorter time intervals over $t' \in [0, \mathfrak{T}]$ and $t' \in [T_{total}, \mathfrak{T}]$, respectively. We then devise strategies to achieve faster numerical computations while maintaining model accuracy, particularly near the beginning of the practical (or useful) prediction zone, with the aim of enhancing the accuracy of continuous wave prediction.

The development of the numerical modeling setups entails an in-depth analysis of the prespecified direction and frequency bandwidths. The major findings are as follows. (1) It is suggested that the direction bandwidth should contain at least 90% of the energy to provide accurate wave predictions in the directional wave field. (2) When the

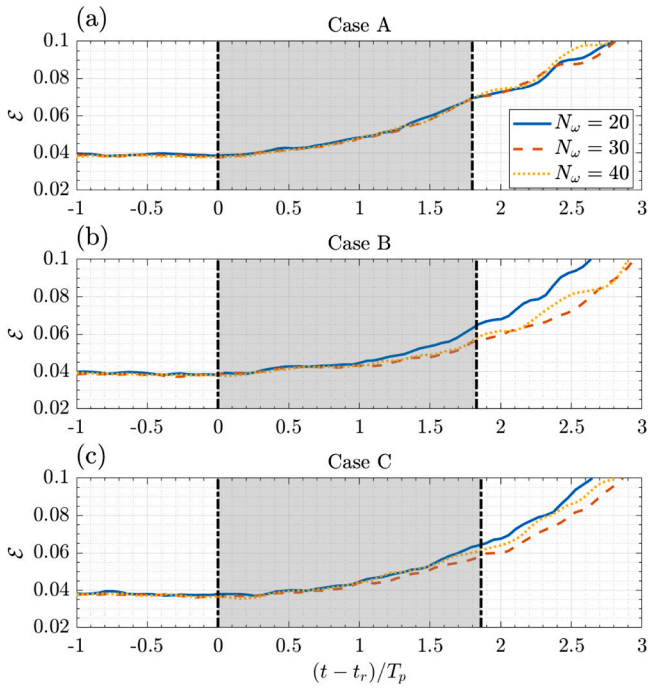

Fig. 11. Temporal evolution of prediction error using ICWM with the optimal frequency domain at WG21 (a) Case A; (b) Case B; (c) Case C (——: N_ω = 20; – – -: N_ω = 30; ·····: N_ω = 40; —·—: boundaries of practical prediction zone; gray shading: practical prediction zone).

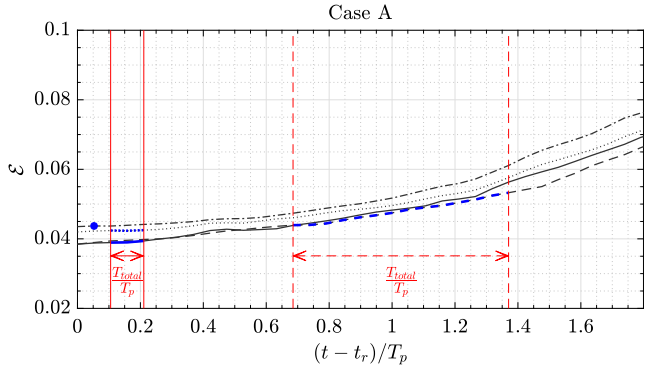

Fig. 12. Temporal evolution of prediction error in the continuous wave forecast for Case A at WG21 where the intervals used in the continuous wave forecast are indicated in blue (——: present ICWM; – – -: previous ICWM; ·····: present LWT-CDR; —·—: present LWT).

frequency domain reaches a certain level for accurate wave descriptions (i.e., $k_{N_\omega} = 12k_p$), increasing the number of components results in an extension to the temporal prediction zone rather than a lower prediction error near the start of the practical zone, ultimately leading to a lower time-averaged prediction error. (3) Using an extensive domain in both frequency and direction may result in deteriorated model accuracy due to excessive nonlinear effects.

In reality, the computation time is likely to increase slightly due to the low quality of assimilated wave measurements, which may include wave shadowing and noise. Future work will involve handling incomplete wave data and addressing the challenges of the real-time collection of actual data.

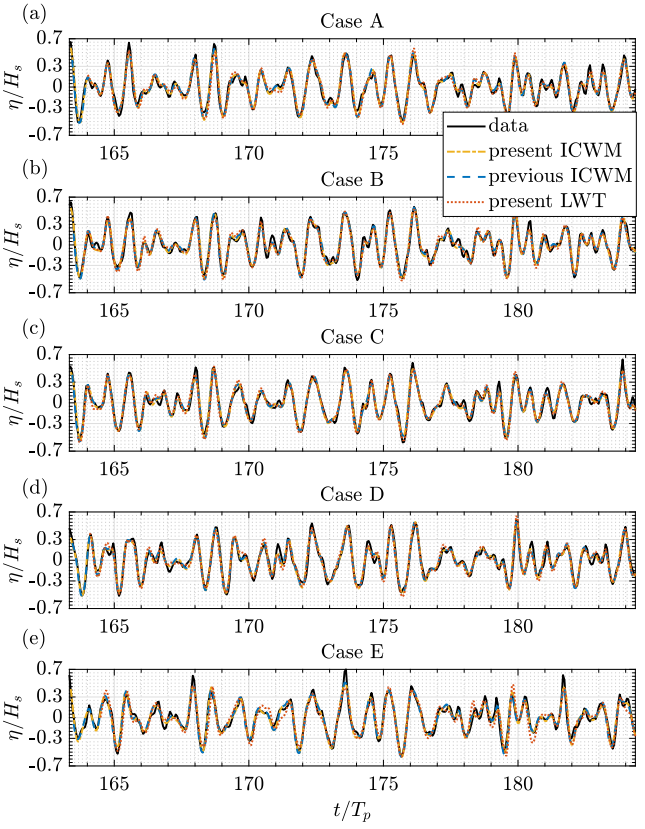

Fig. 13. Time series of surface elevation at WG21: (a) Case A; (b) Case B; (c) Case C; (d) Case D; (e) Case E (——: data; – – -: present ICWM; ·····: previous ICWM; —·—: present LWT).

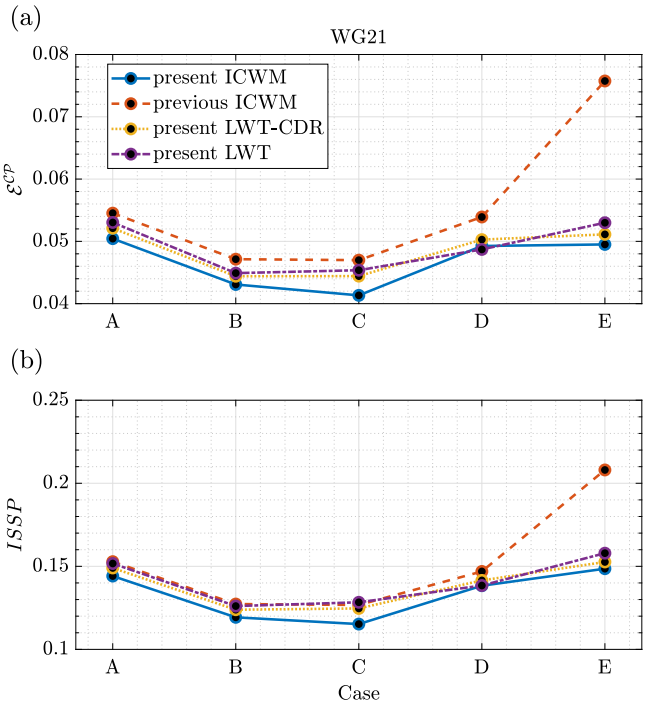

Fig. 14. Comparison of normalized misfit error and ISSP for continuous wave prediction for all the cases at WG21 (——: present ICWM; – – -: previous ICWM; ·····: present LWT-CDR; —·—: present LWT).

CRediT authorship contribution statement

I.-C. Kim: Conceptualization, Investigation, Methodology, Software, Validation, Writing – original draft. **G. Ducrozet:** Project administration, Conceptualization, Methodology, Investigation, Writing – review & editing, Supervision. **V. Leroy:** Conceptualization, Methodology, Investigation, Writing – review & editing, Supervision. **F. Bonnefoy:** Conceptualization, Methodology, Investigation, Writing – review & editing, Supervision. **Y. Perignon:** Project administration, Conceptualization, Methodology, Investigation, Writing – review & editing, Supervision. **S. Bourguignon:** Methodology, Investigation, Writing – review & editing.

Declaration of competing interest

The authors declare that they have no known competing financial interests or personal relationships that could have appeared to influence the work reported in this paper.

Data availability

Data such as experimental datasets and prediction results are openly available at https://doi.org/10.5281/zenodo.7689781 repository.

Acknowledgments

This work was done within the framework of the European H2020 FLOATECH project, Grant agreement ID: 101007142. The authors acknowledge the support of the French Agence Nationale de la Recherche (ANR), under grant ANR-20-CE05-0039 (project CREATIF). The authors also thank the experimental team at LHEEA/Centrale Nantes-CNRS who contributed to the experimental campaign and the corresponding database.

References

Al, M., Fontanella, A., van der Hoek, D., Liu, Y., Belloli, M., van Wingerden, J.W., 2020. Feedforward control for wave disturbance rejection on floating offshore wind turbines. In: Journal of Physics: Conference Series, Vol. 1618, No. 2. IOP Publishing, 022048.

Al-Ani, M., Christmas, J., Belmont, M., Duncan, J., Duncan, J., Ferrier, B., 2019. Deterministic sea waves prediction using mixed space–time wave radar data. J. Atmos. Ocean. Technol. 36 (5), 833–842.

Blondel, E., Bonnefoy, F., Ferrant, P., 2010. Deterministic non-linear wave prediction using probe data. Ocean Eng. 37 (10), 913–926.

Bonnefoy, F., Delacroix, S., Ducrozet, G., Kim, I., Leroy, V., 2023. FLOATECH Project database. Zenodo, http://dx.doi.org/10.5281/zenodo.7689781, Funded by European Commission, project FLOATECH, grant 101007142.

Dannenberg, J., Hessner, K., Naaijen, P., van den Boom, H., Reichert, K., 2010. The on board wave and motion estimator OWME. In: The Twentieth International Offshore and Polar Engineering Conference. OnePetro, pp. 424–431.

Dean, R.G., Dalrymple, R.A., 1991. Water Wave Mechanics for Engineers and Scientists, Vol. 2. world scientific publishing company.

Desmars, N., Bonnefoy, F., Grilli, S., Ducrozet, G., Perignon, Y., Guérin, C.-A., Ferrant, P., 2020. Experimental and numerical assessment of deterministic nonlinear ocean waves prediction algorithms using non-uniformly sampled wave gauges. Ocean Eng. 212, 107659.

Duan, W., Ma, X., Huang, L., Liu, Y., Duan, S., 2020. Phase-resolved wave prediction model for long-crest waves based on machine learning. Comput. Methods Appl. Mech. Engrg. 372, 113350.

Grilli, S.T., Guérin, C.A., Goldstein, B., 2011. Oceanwave reconstruction algorithms based on spatio-temporal data acquired by a flash LiDAR camera. In: The Twenty-First International Offshore and Polar Engineering Conference. OnePetro, pp. 275–282.

Guérin, C.A., Desmars, N., Grilli, S.T., Ducrozet, G., Perignon, Y., Ferrant, P., 2019. An improved Lagrangian model for the time evolution of nonlinear surface waves. J. Fluid Mech. 876, 527–552.

Hilmer, T., Thornhill, E., 2015. Observations of predictive skill for real-time deterministic sea waves from the WaMoS II. In: OCEANS 2015-MTS/IEEE Washington. IEEE, pp. 1–7.

Kabel, T., Georgakis, C.T., Zeeberg, A.R., 2019. Mapping ocean waves using new LIDAR equipment. In: Proceedings of the Twenty-Ninth (2019) International Ocean and Polar Engineering Conference. International Society of Offshore and Polar Engineers, pp. 2258–2562.

Kim, I.C., Ducrozet, G., Bonnefoy, F., Leroy, V., Perignon, Y., 2023. Real-time phase-resolved ocean wave prediction in directional wave fields: Enhanced algorithm and experimental validation. Ocean Eng. 276, 114212.

Klein, M., Dudek, M., Clauss, G.F., Ehlers, S., Behrendt, J., Hoffmann, N., Onorato, M., 2020. On the deterministic prediction of water waves. Fluids 5 (1), 9.

Köllisch, N., Behrendt, J., Klein, M., Hoffmann, N., 2018. Nonlinear real time prediction of ocean surface waves. Ocean Eng. 157, 387–400.

Kurnia, R., Ducrozet, G., 2023. NEMOH: Open-source boundary element solver for computation of first- and second-order hydrodynamic loads in the frequency domain. Comput. Phys. Comm. 292, http://dx.doi.org/10.1016/j.cpc.2023.108885.

Kusters, J., Cockrell, K., Connell, B., Rudzinsky, J., Vinciullo, V., 2016. FutureWaves™: A real-time ship motion forecasting system employing advanced wave-sensing radar. In: OCEANS 2016 MTS/IEEE Monterey. IEEE, pp. 1–9.

Law, Y., Santo, H., Lim, K., Chan, E., 2020. Deterministic wave prediction for unidirectional sea-states in real-time using Artificial Neural Network. Ocean Eng. 195, 106722.

Lee, J.H., Nam, Y.S., Kim, Y., Liu, Y., Lee, J., Yang, H., 2022. Real-time digital twin for ship operation in waves. Ocean Eng. 266, 112867.

Leroy, V., Delacroix, S., Merrien, A., Bachynski-Polić, E., Gilloteaux, J.-C., 2022. Experimental investigation of the hydro-elastic response of a spar-type floating offshore wind turbine. Ocean Eng. 255, 111430.

Li, G., Weiss, G., Mueller, M., Townley, S., Belmont, M.R., 2012. Wave energy converter control by wave prediction and dynamic programming. Renew. Energy 48, 392–403.

Ma, Y., Sclavounos, P.D., Cross-Whiter, J., Arora, D., 2018. Wave forecast and its application to the optimal control of offshore floating wind turbine for load mitigation. Renew. Energy 128, 163–176.

Mitsuyasu, H., Tasai, F., Suhara, T., Mizuno, S., Ohkusu, M., Honda, T., Rikiishi, K., 1975. Observations of the directional spectrum of ocean WavesUsing a cloverleaf buoy. J. Phys. Oceanogr. 5 (4), 750–760.

Naaijen, P., Trulsen, K., Blondel-Couprie, E., 2014. Limits to the extent of the spatio-temporal domain for deterministic wave prediction. Int. Shipbuild. Prog. 61 (3–4), 203–223.

Naaijen, P., Van Oosten, K., Roozen, K., van't Veer, R., 2018. Validation of a deterministic wave and ship motion prediction system. In: International Conference on Offshore Mechanics and Arctic Engineering, Vol. 51272. American Society of Mechanical Engineers, V07BT06A032.

Nouguier, F., Grilli, S.T., Guérin, C.A., 2013. Nonlinear ocean wave reconstruction algorithms based on simulated spatiotemporal data acquired by a flash LIDAR camera. IEEE Trans. Geosci. Remote Sens. 52 (3), 1761–1771.

Nouguier, F., Guérin, C.A., Chapron, B., 2009. "Choppy wave" model for nonlinear gravity waves. J. Geophys. Res. Ocean. 114 (C9).

Perlin, M., Bustamante, M.D., 2016. A robust quantitative comparison criterion of two signals based on the Sobolev norm of their difference. J. Eng. Math. 101 (1), 115–124.

Pierson, Jr., W.J., Moskowitz, L., 1964. A proposed spectral form for fully developed wind seas based on the similarity theory of SA Kitaigorodskii. J. Geophys. Res. 69 (24), 5181–5190.

Previsic, M., Karthikeyan, A., Lyzenga, D., 2021. In-ocean validation of a deterministic sea wave prediction (DSWP) system leveraging X-band radar to enable optimal control in wave energy conversion systems. Appl. Ocean Res. 114, 102784.

Qi, Y., Wu, G., Liu, Y., Kim, M.H., Yue, D.K., 2018a. Nonlinear phase-resolved reconstruction of irregular water waves. J. Fluid Mech. 838, 544–572.

Qi, Y., Wu, G., Liu, Y., Yue, D.K., 2018b. Predictable zone for phase-resolved reconstruction and forecast of irregular waves. Wave Motion 77, 195–213.

Raach, S., Schlipf, D., Sandner, F., Matha, D., Cheng, P.W., 2014. Nonlinear model predictive control of floating wind turbines with individual pitch control. In: 2014 American Control Conference. IEEE, pp. 4434–4439.

Zhang, C., Chen, Z., Zhao, C., Chen, X., Wei, Y., He, J., 2022a. Deterministic sea wave prediction based on least squares with regularization algorithm using coherent microwave radar. IEEE Trans. Geosci. Remote Sens..

Zhang, J., Zhao, X., Jin, S., Greaves, D., 2022b. Phase-resolved real-time ocean wave prediction with quantified uncertainty based on variational Bayesian machine learning. Appl. Energy 324, 119711.